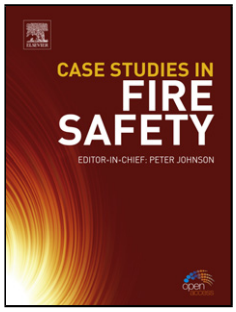

Title: Corrosion Inhibition of Aluminium Alloy AA6063-T5 by Vanadates: Local Surface Chemical Events Elucidated by Confocal Raman Micro-Spectroscopy

Authors: Dmitry S. Kharitonov, Jens Sommertune, Cem Örnek, Jacek Ryl, Irina I. Kurilo, Per M. Claesson, Jinshan Pan

PII: S0010-938X(18)31112-0
DOI: https://doi.org/10.1016/j.corsci.2018.12.011
Reference: CS 7805

To appear in:

Received date: 18 June 2018
Revised date: 22 November 2018
Accepted date: 3 December 2018

Please cite this article as: Kharitonov DS, Sommertune J, Örnek C, Ryl J, Kurilo II, Claesson PM, Pan J, Corrosion Inhibition of Aluminium Alloy AA6063-T5 by Vanadates: Local Surface Chemical Events Elucidated by Confocal Raman Micro-Spectroscopy, *Corrosion Science* (2018), https://doi.org/10.1016/j.corsci.2018.12.011

Corrosion Inhibition of Aluminium Alloy AA6063-T5 by Vanadates: Local Surface Chemical Events Elucidated by Confocal Raman Micro-Spectroscopy

Dmitry S. Kharitonov[a,b,*], Jens Sommertune[c], Cem Örnek[a], Jacek Ryl[d], Irina I. Kurilo[e], Per M. Claesson[a,c,z], and Jinshan Pan[a]

[a]Division of Surface and Corrosion Science, Department of Chemistry, School of Engineering Sciences in Chemistry, Biotechnology and Health, KTH Royal Institute of Technology, SE-100 44 Stockholm, Sweden

[b]Department of Chemistry, Electrochemical Production Technology and Materials for Electronic Equipment, Chemical Technology and Engineering Faculty, Belarusian State Technological University, 220006 Minsk, Belarus

[c]RISE Research Institutes of Sweden, Surface, Process and Formulation, SE-114 86 Stockholm, Sweden

[d]Department of Electrochemistry, Corrosion and Materials Engineering, Gdansk University of Technology, 11/12 Narutowicza st., 80-233, Gdansk, Poland

[e]Department of Physical, Colloid and Analytical Chemistry, Organic Substances Technology Faculty, Belarusian State Technological University, 220006 Minsk, Belarus

[*]**Corresponding authors**:

Dmitry S. Kharitonov: kharitonov@belstu.by

Per M. Claesson: percl@kth.se

Highlights

- *In-situ* and *ex-situ* confocal Raman measurements revealed chemical states of vanadium compounds;
- The inhibition effect is mostly provided by a polymerized film with mixed V(V) and V(IV) species;
- Intermetallic particles in the alloy have a strong influence on the vanadate inhibition process;
- Deposition of polymerized vanadate compounds is mainly connected with micrometer-sized IMPs;

- The inhibition mechanism involves first reduction and then re-oxidation of the vanadium species.

Abstract

Chemical interactions between aqueous vanadium species and aluminium alloy AA6063-T5 were investigated in vanadate-containing NaCl solutions. Confocal Raman and X-ray photoelectron spectroscopy experiments were utilised to gain insight into the mechanism of corrosion inhibition by vanadates. A greenish-grey coloured surface layer, consisting of V^{+4} and V^{+5} polymerized species, was seen to form on the alloy surface, especially on top of cathodic micrometre-sized IMPs, whereby suppressing oxygen reduction kinetics. The results suggest a two-step mechanism of corrosion inhibition in which V^{+5} species are first reduced to V^{+4} or V^{+3} species above cathodic IMPs, and then oxidized to mixed-valence V^{+5}/V^{+4} polymerized compounds.

Keywords: A. Aluminium, **A.** Alloy, **B.** Raman Spectroscopy, **B.** SEM, **B**. XPS, **C.** Vanadate Inhibitor

Introduction

Corrosion protection schemes based on vanadium compounds have been extensively studied in recent years [1–10]. In particular, soluble vanadates [3,5,7], vanadate-based conversion coatings [6,11], pigments [12,13], ion-exchange primers and layered double hydroxides filled with vanadates [14–17] have shown good inhibition performance towards the suppression of localized corrosion of Al alloys. The aqueous solution chemistry of vanadium compounds is quite complex, and dissolved vanadates can undergo a number of hydrolysis, condensation and redox reactions depending on the concentration, pH, temperature and ionic strength of the solution [9,18–24], which complicates elucidation of the exact mechanism of corrosion inhibition. So far, most studies have focused on the speciation of vanadate ions in aqueous solutions [5,8–10,24,25], and the effectiveness of corrosion inhibition has been reported to be strongly dependent on the presence of tetrahedrally-coordinated V^{+5} anions such as VO_4^{3-}, $V_2O_7^{4-}$ and $(VO_3)_n^{n-}$ [1,2,8–10,24–27]. Such anions decrease the kinetics of the cathodic oxygen reduction reaction, which is the dominant cathodic reaction in the corrosion process at near-neutral pH, thereby suppressing the coupled anodic reactions, such as Al dissolution and de-

alloying of Mg from Al_2CuMg (*S*-phase) intermetallic particles (IMPs) in alloy AA2024 [1,2,5,8,9]. As a consequence, this counteracts further increase of copper concentration in such IMPs and thus formation of cathodic Cu-rich clusters that would have been active sites for the oxygen reduction reaction [1,8,28]. However, for other types of Al alloys, for example AA6063, vanadates have been reported to provide a mixed inhibition [4,7,10].

The speciation of aqueous vanadate compounds has been extensively studied and several mechanisms have been proposed, but the interaction of vanadates with metal surfaces has remained less understood [3,5,9,24,26]. For instance, Guan et al. reported that vanadium in its oxidation state +5, in the form of hydrated $VO(OH)_3(OH_2)_2$, initially adsorbs on the surface and then spontaneously polymerizes to form a hydrated vanadium oxide layer during conversion treatment [6]. Furthermore, Iannuzzi *et al*. observed that vanadate species can adsorb on the surface of alloy AA2024-T3 following a Langmuir isotherm, and they concluded that a monolayer of adsorbed vanadates in unknown oxidation states led to the corrosion inhibition [5]. An alternative mechanism was proposed by Ralston *et al*. who reported that the interaction of tetrahedrally-coordinated vanadate ions occurred primarily with *S*-phase intermetallics, but no identification of adsorbed surface species was reported [8,9]. Vanadate species were proposed to have reduced from +5 to +4 oxidation state above Cu-rich IMPs [24,26]. Recently, Feng *et al*. studied the corrosion inhibition of Mg alloy AZ31 in $NaVO_3$/NaCl solutions and proposed a reductive adsorption mechanism of inhibition [27]. The presence of V^{+5}, V^{+4} and V^{+3} species on the surface was confirmed by X-ray photoelectron spectroscopy (XPS). The latter is similar to what has been observed in vanadium-based catalysts, which have been used extensively in organic conversion processes [29–34].

The mechanism of corrosion inhibition in relation to the state of vanadium in the surface-protective film on low-copper containing aluminium alloys has, to our knowledge, not been reported. Raman spectroscopy is a powerful tool for identification and characterization of the structure of vanadium species in aqueous solutions as well as at surfaces [18,24,26,33,35–40]. *In-situ* Raman spectroscopy is a very powerful technique to study a metal surface during its corrosion in aggressive environments, despite lateral and depth resolution limitations of the order of 1 µm. In particular, *in-situ* Confocal Raman Microscopy (CRM) has been employed for identification of vanadium compounds presented in surface layers and for monitoring their changes during chemical processes [41,42]. Utilization of the *in-situ* analytical technique allows direct identification of surface compounds and minimizes the contact with atmospheric oxygen, being reported to influence the oxidation state of adsorbed vanadate species [24].

In our previous work [7] a detailed microstructure characterization of aluminium alloy AA6063-T5, was provided in order to better understand localized corrosion phenomena. It was further shown that the vanadates provided mixed corrosion inhibition effects, mitigating both oxygen reduction on IMPs and anodic dissolution reaction in chloride-containing environment. In this paper, one step further towards understanding the inhibition mechanism of vanadates have been taken and *in-situ* CRM data in aqueous 0.05 M NaCl with and without the vanadate inhibitor are presented and discussed. Local surface distribution and speciation of the vanadate inhibitor have been determined, aiming at elucidation of the corrosion inhibition mechanism at the microscopic scale.

Experimental

Materials.– Aluminium alloy AA6063-T5 was supplied as an extruded sheet material by Taspo Radiotors (Minsk, Belarus). The nominal chemical composition of the alloy is given as (wt.-%): 0.45 Si, 0.50 Fe, 0.10 Cu, 0.10 Mn, 0.60 Mg, 0.1 Cr, 0.15 Ti, and Al (balance). Specimens in sizes of 20 mm × 20 mm × 2.5 mm were cut from thw sheet and used in all experiments. The samples used for CRM and XPS were ground down to 1200-grit using SiC sandpapers, rinsed with deionized water, and then dried in air. The samples used for microstructure characterization were further electropolished in an electrolyte mixture composed of 20 vol.-% perchloric acid and 80 vol.-% ethanol at 20 V and –15 °C for 30 seconds. For corrosion tests, 0.05 M NaCl and 0.05 M NaCl + 3 mM $NaVO_3$ solutions were prepared from chemically pure $NaVO_3$ (≥ 98%) and NaCl (≥ 99%), provided by Sigma-Aldrich. Purified water with 18.2 MΩ-cm resistivity (Milli-Q system) was used for preparation of the solutions as well as rinsing of the samples. The solution with $NaVO_3$ was, prior to experiments, stored for 24 hours in order to reduce the influence of non-equilibrium conditions on the speciation of vanadate ions. The pH was intentionally not adjusted since even slow droplet addition of dilute acid can cause high local acidification with uncontrollable change of vanadate speciation [9,22,24,43]. The pH of the solutions was measured by an automatic titration system Schott Titroline Easy (Sl Analytics, Germany). Vanadium (III, IV and V) oxides and NH_4VO_3 (all ≥ 98%) were obtained from Belreachim and used to obtain Raman reference spectra. The $VO(SO_4)$ reference solution was synthesized from V_2O_5 using the following reaction [44]:

$$V_2O_5 + 2H_2SO_4 + H_2C_2O_4 \rightarrow 2VOSO_4 + 2CO_2 + 3H_2O \qquad (1)$$

Microstructure characterisation.– Scanning electron microscopy (SEM) and energy-dispersive X-ray spectroscopy (EDX) analyses were performed for microstructure characterisation of as-polished samples using a *JEOL JSM-7001F* instrument, equipped with an *Oxford Instruments XMax* EDX Silicon Drift Detector with 80 mm² window size. EDX maps were recorded at 3.5–10 kV accelerating voltage and high probe current over tens of minutes to obtain chemical information with high spatial resolution.

Post-exposure surface examination. The surface of two electropolished specimens was indented with two fiducial markers as a point of reference for SEM analyses. Then one sample was immersed in 100 mL 0.05 NaCl solution and the other was immersed in 0.05 NaCl with 3 mM $NaVO_3$ inhibitor under ambient conditions. Both samples were removed from the respective solution after 1 hour, gently rinsed with deionized water, dried in air, and then examined in an FEI Nova 400 SEM equipped with an Everhart-Thornley detector (ETD) and a through-the-lens (TLD) detector. The ETD was used to gather information from the surface with crystallographic information whereas the TLD was used to show the outermost surface (a few nm's). After the SEM analyses, the samples were again immersed into the solutions and exposed for further 23 hours. The experiments were terminated after 24 hours of total immersion time and the samples were examined again in the SEM. All samples were analysed within 2 hours upon removal from the solutions.

Calculation of vanadium speciation in aqueous solutions.– The predominance and fractional chemical equilibrium diagrams for vanadium species in aqueous solution were calculated using the *Medusa* Software (KTH Royal Institute of Technology, Sweden) based on the SOLGASWATER algorithm with 200 calculation steps along each axis. Values of the thermodynamic equilibrium constants were obtained from the embedded *Hydra* database. The conditions used for the calculation were chosen to represent those used experimentally. This establishes the solution speciation at equilibrium that then can be compared with the vanadium compounds identified on the alloy surface.

Post-immersion XPS analysis.– High resolution XPS analysis was performed on AA6063-T5 samples directly after exposure to 0.05 M NaCl + 3 mM $NaVO_3$ electrolyte for 6 hours. The following exposure to atmospheric air was minimized and lasted less than 120 seconds. XPS spectra were registered using an Escalab 250Xi spectrometer from ThermoFisher Scientific, equipped with an Al Kα X-Ray source (spot size 250 μm), operating at a pass energy of 10 eV and an energy step size of 0.05 eV. Charge compensation was provided by means of a

flood gun, with final calibration performed for adventitious carbon at the C1s peak (BE = 284.6 eV) [45,46]. The Avantage software from ThermoFisher Scientific was used for peak deconvolution.

In-situ and ex-situ CRM analysis.– CRM measurements were performed using a WITec alpha 300 system (WITec GmbH, Germany) equipped with a 532 nm green excitation laser and tubular lens with focal distance of 164.5 mm. The system used has 0.5 microns lateral resolution and 0.7 in depth resolution limitations. The spectra were recorded using a 60× water-immersion objective lens for *in-situ* measurements and 20–100× objective lenses for *ex-situ* scans. Typical integration times were in the range of 0.2 s. The data was analyzed using the Witec Project Plus 4.1 software. Cluster analysis followed by de-mixing was performed in order to distinguish different chemical components, which allowed construction of spatial distribution bitmaps for these components. The bitmaps were overlapped into composite pixel patterns to visualize the distribution of the components over the analyzed areas.

In-situ CRM measurements were performed on 1200-grit ground samples upon immersion in aqueous 0.05 M NaCl and 0.05 M NaCl + 3 mM $NaVO_3$ solutions for 6 and 24 hours, respectively, in order to identify the changes in vanadate speciation with time. Moreover, *in-situ* CRM depth scans along several lines were performed to gain further insights into the mechanism of the vanadate film formation at selected local sites. *Ex-situ* CRM mapping was also done after 24 hours of immersion to check the effect of oxidation in air. In this case, the samples were removed from the solution, gently rinsed with Milli-Q water, and then scanned immediately in lab-air environment. All *in-situ* and *ex-situ* Raman measurements were replicated on two different areas of two different samples.

Results and discussion

Microstructure. An overview of the microstructure is given in Figure 1a, showing the presence of numerous secondary phases finely dispersed within the entire grain structure, with Figure 1b,c showing small and large IMPs. In our previous works [7,47], a comprehensive microstructure characterization was provided and it was shown that secondary phases in AA6063–T5 mainly consisted of micrometre-sized Fe-rich $Al_{4.01}MnSi_{0.74}$, $Al_{1.69}Mg_4Zn_{2.31}$, and $FeAl_3$ intermetallic phases as well as nanometre-sized $CuAl_2$, $ZnAl_2$, and Mg_2Si precipitates. The majority of the micrometre-sized phases were enriched in Fe, Mn, and Si, as those shown in

Figure 1b,c. Such microstructure precipitates in AA6063-T5 were shown to be active sites for the corrosion initiation and propagation [7,47] and, thus, they are in focus in the present study.

Aqueous chemistry of vanadate compounds. The pH of the as-prepared 0.05 M NaCl solution was 6.5–6.7, and it decreased to ≈ 6 after 24 hours of corrosion testing. The solution with 3 mM $NaVO_3$ addition was colourless and had an initial pH of 7.2. The absence of colour indicated the formation of tetrahedrally-coordinated V^{+5} vanadate species during the dissolution of $NaVO_3$ with no clear signs observed for other compounds [9].

Figure 2 shows a fraction diagram for vanadium speciation and a computed potential-pH diagram for the studied solutions. The fraction diagram (Figure 2a) was calculated without any external potential. The results represent equilibrium fractions of the components corresponding to the initial aqueous condition. The diagram shows that the aqueous vanadate speciation is rather complex and strongly pH-dependent. Only V^{+5} species are formed in 0.05 M NaCl solution under the conditions used in the calculation. Tetrahedral monovanadate $VO_2(OH)_2^-$, trivanadate $V_3O_9^{3-}$, tetravanadate $V_4O_{12}^{4-}$, and octahedral decavanadate ions ($V_{10}O_{28}^{6-}$ and $V_{10}O_{27}(OH)^{5-}$) are the predicted stable species at around pH 6. It has been reported [48] that in near-neutral solutions cyclic trimers $V_3O_9^{3-}$ are rapidly converted to tetramers $V_4O_{12}^{4-}$. Gradual alkalization to pH ≈ 9, which is possible at cathodic areas during the corrosion process [49,50], can lead to the formation of other V^{+5} species such as $VO_3(OH)^{2-}$ and $HV_2O_7^{3-}$. Only monomeric vanadate $VO_3(OH)^{2-}$ species are present above pH 10. A decrease in pH to 3–6 is possible at anodic sites due to local acidification as a result of hydrolysis of dissolved metal ions [49–51], and this may lead to polymerization into different types of polyvanadate ions.

The eventual influence of the corrosion product Al^{3+} on the speciation of vanadium compounds in the solution was also considered in the calculations. Initial concentrations of Al^{3+} in the range of 0.1 – 1000 mM were used as input parameter for the calculation, but in all cases only corrosion products in form of insoluble $Al(OH)_3$ were predicted in the pH range 4–10. Formation of V–Al compounds in aqueous solutions at ambient temperature is thermodynamically unfavourable [52,53].

When the alloy is immersed in the solution containing the vanadate, anodic and cathodic electrochemical reactions at the alloy surface and homogeneous chemical reactions in the liquid phase may take place. The OCP of the AA6063-T5 alloy in this solution approaches

≈ –0.41 V_{SHE} [7], and hence the vanadate speciation near the alloy surface can be altered. At this potential vanadate species get spontaneously reduced to the V(III) oxide V_2O_3 according to the calculated equilibrium E-pH diagram shown in Figure 2b. Note that during the corrosion process the system is not in equilibrium, however, it strives towards equilibrium and the calculations show towards which state the system is moving. The V^{+3} compounds are strong reducing agents which are stable only in de-aerated solutions over limited pH and potential ranges [19,21,54]. In contrast, in aerated solutions V^{+3} species have been reported to become rapidly oxidized by dissolved oxygen, leading to the formation of more thermodynamically stable V^{+4} compounds [21]. Our confocal Raman spectroscopy and XPS measurements detected both V^{+4} and V^{+5} compounds at the alloy surface, suggesting that oxidation of V^{+3} compounds by dissolved oxygen may have occurred under the experimental conditions.

Post-corrosion SEM analyses.

Figure 3 shows SEM micrographs of the same surface area before and after immersion in 0.05 M NaCl solution without the inhibitor. Microstructural details, such as grain boundaries and IMPs, could be easily discerned before immersion in the solution. Furthermore, some nanometre-sized globular features were seen on some micrometre-sized IMPs (Figure 3d). These features were not seen when the alloy was examined for microstructure characterization (Figure 1), but must have been formed during storage in ambient air environment and are denoted as oxidation products in this report.

The sample suffered from corrosion during exposure to the aqueous NaCl solution. Numerous corrosion products were formed on the surface already after 1 hour of immersion, as shown in Figure 3, and the grain orientation was obscured by the corrosion attack. SEM analyses with higher magnification revealed small particles on the surface that are likely corrosion products. The corrosion attack was more pronounced after 24 hours of immersion (Figure 3). Localized attack on the periphery of some large IMPs was observed (Figure 3b–d), and corrosion products were precipitated in the vicinity of these intermetallics. The surface became rougher and large IMPs protruded more from the surface, which suggests preferential metal dissolution of the matrix around the IMPs. The dissolution rate on adjacent sites to the IMPs was significantly higher than on other regions of the surface. Corrosion most likely initiated at the IMP/matrix interface, proceeded along the interphase regions and extended towards the matrix. However, some selective localized attack was also seen on the IMPs (Figure 3d). The extent of the localized attack varied for different IMPs (Figure 3b-c), indicating electrochemical nobility variations among these secondary phases, which is in-line with the Volta potential data presented

in our previous studies [7,47]. The observed localized corrosion is also consistent with micro-galvanic corrosion, being typically triggered by relatively large cathodic type IMPs in Al alloys [49,51,55].

On the contrary, no pronounced corrosion attack was observed, neither general nor localized, after the immersion in 0.05 M NaCl with 3 mM $NaVO_3$ (Figure 4). Until the termination of the experiment, the grain orientation contrast was preserved and no significant change in the IMP/matrix interphase was observed after 24 hours of exposure, which clearly showed the corrosion inhibition effect of vanadate species in the chloride-containing electrolyte. Only minor corrosion products were observed on a few discrete sites as illustrated in Figure 4b.

Post-immersion XPS analysis. The XPS analysis was performed in order to elucidate the vanadate chemical states on the surface of the aluminum alloy as a result of 6 hours of exposure to 0.05 M NaCl with 3mM $NaVO_3$ electrolyte. High-resolution XPS spectra were recorded in the binding energy (BE) range of the *Al2p, V2p,* and *O1s* peaks in order to differentiate between various chemical states. The results are presented in Figure 5a–c.

Figure 5a refers to the *V2p* spectrum, registered at the surface of the sample. The spectra was deconvoluted into two peak doublets, where BE (517.2 eV) of the primary component is characteristic for the +5 oxidation state of vanadium [24,76,77]. A smaller component ascribed to the +4 oxidation state was also identified [26, 27]. The relative V^{+5} : V^{+4} ratio was 6.5 : 1. The deconvolution of the *Al2p* high-resolution XPS spectra, presented on Figure 5b, was carried out using two peak doublets located in the energy range characteristic for metallic aluminum (72.5 eV) and Al_2O_3 oxides (75.0 ± 0.2 eV), respectively. Finally, the *O1s* spectra revealed the presence of three different chemical states, a feature characteristic for thin oxide layers on metal surfaces, Figure 5c [76,80,81]. The major component, present at 532.7 eV primarily originates from hydroxyl oxygen OH^-, with possible small influence from C–O contamination resulting from exposure to atmospheric air. This peak is typically shifted approximately +1.0 eV versus the metal oxide, O^{-2}, component [80,82]. The last component, observed at significantly higher BE, around 534.3 eV, represents oxygen contained within chemisorbed H_2O molecules [83]. Results of the deconvolution are summarized in Table 1. Similar to other adsorption studies of vanadate oxides on aluminium metal surfaces, in addition to the surface oxide (Al_2O_3), the layer formed in our study is primarily composed of hydroxide precipitates while the amount of chemisorbed water is relatively low, testifying for low corrosion susceptibility of aluminium in presence of vanadate species [76,80].

Reference Raman spectra. The exact assignment of the vanadate-related Raman peaks is complicated because vibrational bands for different vanadium compounds are located very close to each other and can sometimes overlap. The peaks in the Raman spectra were interpreted by comparing the general appearance and peak positions with those reported in the literature for vanadium compounds (Table 2) [18,29–31,38,41,56–68], and with our own reference spectra collected using commercially available vanadium compounds (Figure 6 and Table 2).

For solid vanadium III, IV and V oxides, spectra with intense peaks at 995–993, 686–694 and 410 cm^{-1} were recorded (Figure 6a–c). For the compounds in the V^{+5} oxidation state, typical bands at 932, 902, and 437 cm^{-1} were observed for NH_4VO_3, whereas three strong peaks in the range 950–893 and peaks at 738 and 437 cm^{-1} were noted for $NaVO_3$ (Figure 6d-e). Peaks at 990, 904, 594, 537, 485, 445, and 326 cm^{-1} were detected for the acidic solution containing $VO(SO_4)$, where vanadium is in the oxidation state +4 (Figure 6f). Only two broad bands at 500–640 and 900–1200 cm^{-1}, which are typical for mixtures of V^{+5} polyvanadate ions, were seen in the 0.05 M NaCl + 3 mM $NaVO_3$ solution (Figure 6g).

In-situ CRM analysis. As reported for the AA2024 alloy [1,24,26], and expected from our observations on the AA6063-T5 alloy [7,10], the inhibition efficiency of vanadates is strongly connected to the IMPs. The vanadate species may adsorb on the entire surface, but appears to form precipitates of reaction products mainly on and around large IMPs, serving as active centers with high rate of local electrochemical reactions that generate corrosion products [49,51]. Therefore, regions visually containing large intermetallics, being primarily cathodic with respect to the Al matrix [7,47], were chosen for *in-situ* and *ex-situ* CRM measurements. As an example, Figure 7 shows optical images of such an area obtained after 24 hours of exposure to 0.05 M NaCl + 3 mM $NaVO_3$ solution before and after excessive rinsing with flowing water. Before rinsing, accumulation of vanadate at one given spot was observed as a green-grey area (Figure 7a). After removal of the precipitate layer by rinsing, a large IMP feature was observed on this location (Figure 7b). This confirms the heterogeneous nature of the precipitated vanadium-containing layer, which in particular appeared over some large IMPs. The exact IMP compositions were not determined during the Raman studies, but extensively discussed in our previous publications [7,47], and most of the micrometer-sized IMPs were of Fe-rich Al-Mn-Si-type, as briefly mentioned here (Figure 1). The *in-situ* CRM spectra obtained after 24 hours of immersion in aqueous 0.05 M NaCl solution without vanadate inhibitor showed only one pronounced band at 782 cm^{-1} associated with corrosion products in the form of AlOOH [69].

After 6 hours of immersion in 0.05 M NaCl + 3 mM $NaVO_3$ solution, the vanadium-containing surface layer appeared to have a rather complex chemistry as revealed by CRM (Figure 8). The optical micrograph (Figure 8a) shows a greenish-grey colored precipitate on top of the alloy surface, which is a typical color for V^{+3} and V^{+4} species [19]. Further information about the vanadium compounds was obtained from CRM spectra. Spectrum 8b1 has a weak peak at 970 cm^{-1}, two strong peaks at 953 and 921 cm^{-1} and additional peaks at 633, 510 and 243 cm^{-1}. The relative intensity of the three main peaks in the region 800–1000 cm^{-1} suggests co-existence of vanadium compounds with mixed oxidation state at the analyzed site. As can be seen from Table 2, the band at 970 cm^{-1} can be due to the presence of either decavanadates (V^{+5}) or V^{+4} species. However, the strongest peak at 995 cm^{-1}, typical for decavanadate ions, was not observed. XPS measurements (Figure 5) and thermodynamic calculations (Figure 2) also supports the reduction of V^{+5} species. Thus, the 970 cm^{-1} band is assigned to the V=O stretching vibration of crystalline V^{+4} compounds [67], whereas the other peaks correspond to the V=O and V–O–V vibrations that are typical for poly-vanadate V^{+5} ions such as $V_4O_{12}^{4-}$ and $V_5O_{15}^{5-}$ [18,33,61]. It should be mentioned that the ionic strength of the solution affects the position of the Raman bands by stabilizing vanadate species with high negative charge [36]. Addition of NaCl to a vanadate-containing solution can thus shift the equilibria of V^{+5} species towards a larger *n*-value in $(VO_3)_n^{n-}$ oligomers [70], which in turn can shift the Raman signal to higher frequencies [18]. The non-stoichiometry or structural disorder of the formed vanadium species have also been reported to affect peak positions [65].

The Raman spectra 8b2 and 8b3 (Figure 8b) provide evidence for the presence of polymerized vanadium species. The broad band at 850–980 cm^{-1} has previously been reported as an indicator for two-dimensional distorted polymeric vanadium species [24,26,39,71–74]. The shoulder of the main band at 990 cm^{-1} (spectra 8b2) indicates the presence of a crystalline phase [26,31,35,37,65,68]. According to our data for VO^{2+} (Figure 6) and [38, 67] this band together with the weak peaks at 594 and 320 cm^{-1} are assigned to crystalline polymeric V^{+4} species, which are able to form cross-linked chain structures $(V_2O_4 \times H_2O)_n$ [65]. Other bands are similar to those in the 8b1 spectrum and emanate from V^{+5} species. The absence of sharp peaks in the 8b3 spectrum indicates higher degree of polymerization of the vanadium compounds compared to those giving rise to the 8b2 spectrum. The exact valence state of vanadium in these species remains to be a contentious matter [26]. Reduction of V^{+5} ions to V^{+4} species creates V^{+4}=O bonds that are weaker than V^{+5}=O bonds [39]. Lee *et al.* observed a shift of the broad peak with the highest intensity towards lower frequencies during the reduction process [39]. Thus, the shift

observed for the 8b3 spectrum compared to the 8b2 spectrum suggests an increased amount of V^{+4} species.

The CRM map (Figure 8c) shows enhanced reduction of V^{+5} species and polymerized V^{+4} species distributed across an area most likely containing IMPs (red and green color). An *in-situ* CRM depth scan of the area with a thick precipitate layer, indicated with a dotted line in Figure 8a, is shown in Figure 8d. The vanadium-containing surface film had a locally layer-like structure with a thickness of 6–8 µm. Polymerized V^{+4} vanadate species (green color in the image) were formed in the bottom region where localized corrosion/dissolution may have occurred. The top layer consisted primarily of a mixture of polymerized compounds (red color) with some $V_5O_{15}^{5-}$ ions (yellow color). The blue color represents the alloy surface. The results suggest that, after 6 hours of immersion, a several µm thick and chemically heterogeneous vanadium-rich precipitation layer formed on top of large IMPs.

After 24 hours of immersion, a similar greenish-grey colored vanadate precipitation layer was also observed (Figure 9). The CRM data indicate two typical types of vanadate compounds over different surface regions. Spectrum 9b1 (Figure 9b), extracted from the precipitate layer, shows Raman bands at 944, 835, 695, 434 and 373 cm^{-1}. The peaks at 944 and 695 cm^{-1} are typical for V^{+5} compounds [31,35,37,71,75], where the bands at 835, 434 and 373 cm^{-1} have been observed for V^{+4} species [35,37,38,56]. Thus, the results suggest the formation of mixed V^{+5}/V^{+4} compounds on top of large IMPs [35,37,71,75]. Spectrum 9b2, extracted from a small spot (green area in Figure 9c), exhibits some symmetric and asymmetric stretching vibrations of polymeric tetrahedrally-coordinated species, $(VO_4^{3-})_n$ at 880 and 830 cm^{-1}, respectively. Together with the symmetric δ-vibration of VO_4^{3-} at 355 cm^{-1}, which is common for polymeric V^{+5}–Mg species, these features suggest the presence of $Mg_3(VO_4)_2$ or $Mg_4V_2O_9$ [66,68]. The sharp Raman peaks observed in spectra 9b1 and 9b2 indicate a partially crystalline structure of the precipitate compounds [39].

The CRM map presented in Figure 9c shows that the thick precipitate layer formed over the large IMPs is composed mainly of mixed V^{+5}/V^{+4} compounds, with a small portion of Mg–V compounds. The depth profile in Figure 9d shows that both types of compounds were found at specific surface sites where they were distributed throughout the film. Thicker layers of precipitation products were observed to breakdown or detach from the alloy surface. In summary, according to *in-situ* CRM data, exposure in vanadate-containing solution resulted in

gradual reduction of adsorbed vanadate species and formation of mixed-valence V^{+5}/V^{+4} polyvanadates.

Post-immersion CRM analysis. Results of the *ex-situ* CRM measurements performed immediately after removal from the solution and after 24 hours of aging in air are exemplified in Figure 10. The green-colored surface layer observed *in-situ* (Figure 8, 9) was not observed *ex-situ* (Figure 10a), which suggests removal of a loosely bound vanadate layer during rinsing with deionized water. Two typical CRM spectra (Figure 10b), representing the green and red colors in the CRM map (Figure 10c), were obtained in an area containing large IMPs. Raman signals from vanadate compounds were also detected in the areas of surface defects, such as polishing marks. Spectrum 10b1 shows a broad band at ≈840 cm^{-1} corresponding to polymeric vanadate species, whereas the band at ≈935 cm^{-1} is associated with the distorted V^{+4}=O stretching mode [38, 67]. Spectrum 10b2 shows a broad band at 780–840 cm^{-1}, which is typical for polymeric vanadate species in mainly the +5 oxidation state. Thus, after short time in air both V^{+4} and V^{+5} species were found on the surface. In contrast, polymeric vanadate species primarily in the +5 oxidation state were detected after 24 hours of exposure in air, as shown in Figure 10d–f. Thus, the *ex-situ* CRM measurements confirm that reduced vanadates in the precipitated layer become oxidized into +5 oxidation state during aging in air.

Mechanism of corrosion inhibition of AA6063-T5 by vanadates. Corrosion inhibition by $Me^{n+}O_4^{n-8}$ anions (Me = Cr, Mo, Mn and V) usually involves reduction of the initial inhibitor ions at the metal surface, leading to the formation of protective films of insoluble oxides and/or hydroxides [84–88]. It has been reported that neither vanadates nor molybdates provide inhibition in de-aerated solutions [2,9,87]. Therefore, dissolved oxygen is key for corrosion inhibition, and this implies a second step in the inhibition mechanism that involves oxidation of the initially reduced species. Such a mechanism is similar to the action of V^{+5}-based catalysts. Their catalytic activity is based on the reduction of O_2 and conversion between oxidation states of vanadium from +5 to +4 or +3 and then back to +5 during the catalytic cycle [29,30,32,33,41,71]. A catalyst-like oxidation-reduction mechanism has also been suggested for the inhibition of AA2024 [24] and the Mg alloy AZ31 [27] by vanadates.

Corrosion inhibition is provided mainly by tetrahedrally coordinated V^{+5} aqueous vanadates [1,4,8–10,25], and therefore these species are important at the initial inhibition stage. Previously [8,9,24,26], the inhibition mechanism of vanadates has been strongly connected with the presence of Cu-rich IMPs. Indeed, our previous studies [7,10] and data reported here suggest

high effectiveness of vanadates towards suppression of the corrosion of the low Cu content alloy AA6063–T5. Unlike the XPS or EDX analysis, in which the samples need to be removed from the corrosive medium and dried, our *in situ* CRM results presented in this report allowed us to follow the evolution of the surface vanadate film structure and composition. The data suggests that the inhibition mechanism involves several steps and is strongly associated to the microstructure, especially large IMPs. The proposed steps of the film formation process are schematically illustrated in Figure 11. On the alloy surface, an air-formed Al oxide film may exist as Al is spontaneously oxidized to form a thin oxide film according to the reaction:

$$2Al + 3H_2O \rightarrow Al_2O_3 + 6H^+ + 6e^- \quad (2)$$

However, the presence of large IMPs and lack of a protective oxide film in the boundary regions surrounding the IMPs may trigger localized corrosion [44,50], leading to extensive corrosion attack. With the vanadate inhibitor in the solution, initial adsorption of dissolved V^{+5} species occurs on the surface (Figure 11a,b). The isoelectric point of the native oxide film on Al alloys is about 9.5 [89]. Thus, the surface has an excess positive charge at pH ≈ 6, which promotes adsorption of negatively charged vanadate anions. Being strong oxidants, adsorbed V^{+5} species are spontaneously reduced to V^{+4} species on the surface, especially on local acidic sites:

$$VO_2(OH)_2^- + 2H^+ + e^- \rightarrow VO_2 + 2H_2O, \quad (3)$$

$$V_nO_{3n}^{n-} + 2nH^+ + ne^- \rightarrow nVO_2 + nH_2O \ (n = 3, 4, 5), \quad (4)$$

Further electrochemical reaction can reduce V^{+4} species to V^{+3} species (Figure 2b):

$$2VO_2 + 2H^+ + 2e^- \rightarrow V_2O_3 + H_2O. \quad (5)$$

Note that reduction of initially adsorbed V^{+5} species was considered only over the oxide-free intermetallic particles. This aspect is different from the mechanism reported for the Mg alloy AZ31, where high amount of Mg allows for a reductive adsorption of vanadate over the alloy matrix. The AA6063–T5 alloy contains micrometer-sized cathodic IMPs and some nanometer-sized anodic IMPs, and interphase boundaries are typically anodic [7,47]. Cathodic IMPs can promote reduction reactions, so such reactions take place preferentially on the large IMPs. In the boundary regions, the local pH may decrease as a result of anodic dissolution [49,50], supplying H^+ ions for the above-mentioned reduction reactions. Therefore, the large IMPs could facilitate the electrochemical reduction of high-valence vanadate species. The micro-galvanic corrosion induced by the large cathodic IMPs lead to local enrichment of the reduced vanadate species on top of and around the large IMPs (Figure 11c). However, in aerated aqueous solutions, the reduced V^{+3} species spontaneously become oxidized by dissolved oxygen to V^{+4} species, which are indeed observed by CRM and XPS analysis (Figures 5, 8, 9). The comproportionation reaction, $V^{+3} + V^{+5} \rightarrow 2V^{+4}$, is also possible. Water molecules induce structural changes in the

adsorbed vanadium species, promoting formation of hydrated pseudo-octahedrally coordinated complexes [34,90,91]. The adsorbed V^{+5} vanadate ions lead to corrosion suppression during the first hours [7,10], probably due to their preferential inhibition effect on the reactive sites, i.e., micro-galvanic couples associated to large cathodic IMPs.

Our CRM results provide evidence for the second step in the surface film formation. It includes subsequent oxidation of the reduced V^{+4} species leading to formation of mixed-valence vanadate compounds, which is supported by the oxygen reduction reaction (Figure 11d,e):

$$n\mathrm{VO_2} + \mathrm{H_2O} - 2e^- \rightarrow \mathrm{V_nO_{n+1}} + 2\mathrm{H^+} \quad (n = 3, 4, 6), \qquad (6)$$

$$\mathrm{O_2} + 2\mathrm{H_2O} + 4e^- \rightarrow 4\mathrm{OH^-}. \qquad (7)$$

Several mixed V^{+5}/V^{+4} compounds, for example V_3O_7, V_4O_9 or V_6O_{13}, with different V^{+5}/V^{+4} ratios, could be formed according to Eq. 6 [35,92], and nonstoichiometric mixed phases are observed in the CRM measurements (Figure 8). Since the oxidation and reduction reactions mostly take place on the alloy surface, and are enhanced on the surface of IMPs and the surrounding boundary regions, the microstructure of the alloy has a strong influence on these reactions.

Local acidification due to formation of H^+ in the vicinity of the corroding sites causes polymerization of the adsorbed vanadate species as predicted by the Medusa calculations (Figure 2), leading to formation of oligomers that probably are mixed V^{+5} $\left\{\left[\mathrm{VO(OH)_3(H_2O)_2}\right]\right\}_n$ and V^{+4} $\left\{\left[\mathrm{VO(OH)_2(H_2O)_3}\right]\right\}_m$ species [19–21]. As the degree of oligomerization increases, condensation and local saturation of the vanadium species occur and the film thickness increases, which eventually causes formation of crystalline hydrated mixed-valence vanadium compounds (Figure 11f). Formation of such a layer-like surface film was observed by *in-situ* CRM depth scans already after 6 hours of immersion (Figure 8d). As the film thickness increases, it appears to eventually break down, presumably at the interface between the amorphous and crystalline phases (Figure 11g). Evidence for this was observed after 24 hours of immersion (Figure 9). Such loosely bound vanadate layers cannot provide long-term corrosion protection, in agreement with the weight loss measurements showing a decreasing inhibition efficiency after prolonged time [7]. These results suggest that the initially formed polymerized vanadate film is most important for the inhibition efficiency, which is consistent with data reported for the AA2024 alloy [5].

Our *in-situ* CRM results indicate the formation of a thick vanadate-based film only over large IMPs, which mostly exhibit cathodic character relative to the Al matrix [7,47,93]. They behave as local cathodes [28,87], promoting the reduction reactions of vanadates. Note that the inhibition mechanism over the oxide-covered alloy matrix does not involve the oxidation-reduction reaction of vanadium species as described above. However, it is possible that a very thin vanadate film of V^{+5} species is also formed on the Al matrix surface, which is not thick enough to be detectable by CRM, but readily observed by XPS (Figure 5). The high inhibition efficiency observed in electrochemical measurements [7] suggests the presence of such a very thin inhibitor film on the alloy surface. The low isoelectric point of V^{+5} species (≈2.3) makes further adsorption and growth unfavorable on the alumina-covered surface, and the poor catalytic nature and conductivity of alumina suppresses possible reduction of the adsorbed V^{+5} species [87]. All these features emphasize the important role of the IMPs in the localized corrosion of the Al alloy and the inhibition efficiency of vanadates.

Conclusions

1. No clear signs of corrosion attack on the surface of the aluminium alloy AA6063-T5 was observed after one-day of immersion in 0.05 M NaCl with 3 mM $NaVO_3$. Vanadate species suppressed anodic dissolution reaction of both the Al matrix and IMPs.

2. During immersion of the AA6063-T5 alloy in 3mM $NaVO_3$ + 0.05 M NaCl solution, formation of a micrometer-thick precipitate vanadate film occurred selectively over and around the large cathodic IMPs. Formation of a thin film over the oxide-covered Al matrix is also likely as evidenced by XPS.

3. The vanadate inhibitor provided corrosion inhibition of AA6063-T5 by a complex mechanism, which involves a two-step process, with V^{+5} vanadates being first reduced to V^{+4} or V^{+3} species on the surface of cathodic IMPs followed by a subsequent oxidization with formation of mixed-valence V^{+5}/V^{+4} polymerized compounds. The precipitated vanadate film in the first hours of inhibition has a layered structure with a V^{+5}/V^{+4} polymerized amorphous bottom layer and a crystalline layer of hydrated mixed-valence vanadium compounds, forming the outermost surface.

4. The inhibition effectiveness of vanadates towards AA6063-T5 is mostly provided by the polymerized vanadate film, being formed during the first hours of immersion in the vanadate-

containing solution. The crystalline layer formed later is easily removed from the surface, and, thus, does not contribute to a long-term corrosion protection.

5. Aging in air of the vanadate-pretreated AA6063-T5 alloy surface resulted in oxidation of surface V^{+4} species by oxygen and formation of polymerized V^{+5} species over large IMPs.

Acknowledgements

The authors at Belarusian State Technological University are grateful for the financial support by The Ministry of Education of the Republic of Belarus under the grant no. 20161135. Dmitry Kharitonov gratefully acknowledge financial support from the Swedish Institute (Visby programme PhD scholarship). The authors at KTH Royal Institute of Technology are grateful for the partial financial support by Swedish Foundation for Strategic Research (SSF project RMA11-0090) and the support by Knut and Alice Wallenberg Foundation for the use of the CRM instrument. Jacek Ryl gratefully acknowledge the financial support of the Polish Ministry of Science and Higher Education from the budget funds in the period 2016-2019 under Iuventus Plus project no. IP2015067574.

Data availability

The raw/processed data required to reproduce these findings cannot be shared at this time as the data also forms part of an ongoing study.

References

[1] M. Iannuzzi, G.S. Frankel, Inhibition of aluminum alloy 2024 corrosion by vanadaes: An in situ atomic force microscopy scratching investigation, Corrosion. 63 (2007) 672–688. doi:10.5006/1.3278417.

[2] M. Iannuzzi, J. Kovac, G.S. Frankel, A study of the mechanisms of corrosion inhibition of AA2024-T3 by vanadates using the split cell technique, Electrochim. Acta. 52 (2007) 4032–4042. doi:10.1016/j.electacta.2006.11.019.

[3] K.D. Ralston, R.G. Buchheit, An Initial Exploration of Corrosion Inhibition of AA6061 and AA7075 by Aqueous Vanadates, ECS Electrochem. Lett. 2 (2013) C35–C38. doi:10.1149/2.005309eel.

[4] D.S. Kharitonov, I.I. Kurilo, I.M. Zharskii, Effect of Sodium Vanadate on Corrosion of AD31 Aluminum Alloy in Acid Media, Russ. J. Appl. Chem. 90 (2017) 1089−1097. doi:10.1134/S1070427217070102.

[5] M. Iannuzzi, G.S. Frankel, Mechanisms of corrosion inhibition of AA2024-T3 by vanadates, Corros. Sci. 49 (2007) 2371–2391. doi:10.1016/j.corsci.2006.10.027.

[6] H. Guan, R.G. Buchheit, Corrosion protection of aluminum alloy 2024-T3 by vanadate conversion coatings, Corrosion. 60 (2004) 284–296. doi:10.5006/1.3287733.
[7] D.S. Kharitonov, C. Ornek, P.M. Claesson, J. Sommertune, I.M. Zharskii, I.I. Kurilo, J. Pan, Corrosion Inhibition of Aluminum Alloy AA6063-T5 by Vanadates : Microstructure Characterization and Corrosion Analysis, J. Electrochem. Soc. 165 (2018) 116–126. doi:10.1149/2.0341803jes.
[8] K.D. Ralston, T.L. Young, R.G. Buchheit, Electrochemical Evaluation of Constituent Intermetallics in Aluminum Alloy 2024-T3 Exposed to Aqueous Vanadate Inhibitors, J. Electrochem. Soc. 156 (2009) C135. doi:10.1149/1.3076147.
[9] K.D. Ralston, S. Chrisanti, T.L. Young, R.G. Buchheit, Corrosion Inhibition of Aluminum Alloy 2024-T3 by Aqueous Vanadium Species, J. Electrochem. Soc. 155 (2008) C350. doi:10.1149/1.2907772.
[10] D.S. Kharitonov, I.I. Kurilo, A. Wrzesinska, I.M. Zharskii, Corrosion inhibition of AA6063 alloy by vanadates in alkaline media, Mat.-Wiss. u. Werkstofftech. 48 (2017) 646–660. doi:10.1002/mawe.201600752.
[11] A.S. Hamdy, I. Doench, H. Möhwald, Intelligent self-healing corrosion resistant vanadia coating for AA2024, Thin Solid Films. 520 (2011) 1668–1678. doi:10.1016/j.tsf.2011.05.080.
[12] R.L. Cook Jr., S.R. Taylor, Pigment-Derived Inhibitors for Aluminum Alloy 2024-T3, 56 (2000) 321–333.
[13] D.S. Kharitonov, I.I. Kurilo, I.M. Zharsky, Synthesis and physical-chemical properties of inorganic pigments based on the divalent metals vanadates, Sviridov Readings. 11 (2015) 177–185.
[14] J.M. Vega, N. Granizo, D. De La Fuente, J. Simancas, M. Morcillo, Corrosion inhibition of aluminum by coatings formulated with Al-Zn-vanadate hydrotalcite, Prog. Org. Coatings. 70 (2011) 213–219. doi:10.1016/j.porgcoat.2010.08.014.
[15] Y. Li, S. Li, Y. Zhang, M. Yu, J. Liu, Enhanced protective Zn-Al layered double hydroxide film fabricated on anodized 2198 aluminum alloy, J. Alloys Compd. 630 (2015) 29–36. doi:10.1016/j.jallcom.2014.12.176.
[16] M.L. Zheludkevich, S.K. Poznyak, L.M. Rodrigues, D. Raps, T. Hack, L.F. Dick, T. Nunes, M.G.S. Ferreira, Active protection coatings with layered double hydroxide nanocontainers of corrosion inhibitor, Corros. Sci. 52 (2010) 602–611. doi:10.1016/j.corsci.2009.10.020.
[17] J. Tedim, M.L. Zheludkevich, A.N. Salak, A. Lisenkov, M.G.S. Ferreira, Nanostructured LDH-container layer with active protection functionality, J. Mater. Chem. 21 (2011) 15464–15470. doi:10.1039/c1jm12463c.
[18] M. Aureliano, C.A. Ohlin, M.O. Vieira, M.P.M. Marques, W.H. Casey, L.A.E. Batista de Carvalho, Characterization of decavanadate and decaniobate solutions by Raman spectroscopy, Dalt. Trans. 45 (2016) 7391–7399. doi:10.1039/C5DT04176G.
[19] D.C. Crans, A.S. Tracey, The chemistry of vanadium in aqueous and nonaqueous solution, in: A.S. Tracey, D.C. Crans (Eds.), Vanadium Compd. Chem. Biochem. Ther. Appl., American Chemical Society, Washington DC, 1998: pp. 2–29. doi:10.1021/bk-1998-0711.ch001.
[20] M. Henry, J.P. Jolivet, J. Livage, Aqueous chemistry of metal cations: Hydrolysis, condensation and complexation, in: R. Reisfeld (Ed.), Struct. Bond., Springer-Verlag, Berlin, 1992: p. 153. doi:10.1007/BFb0036968.
[21] D. Rehder, Inorganic and Coordination Compounds of Vanadium, John Wiley & Sons, Chichester, 2008.
[22] J.W. Larson, Thermochemistry of Vanadium(5+) in Aqueous Solutions, J. Chem. Eng. Data. 40 (1995) 1276–1280. doi:10.1021/je00022a030.
[23] J.J. Cruywagen, J.B.B. Heyns, A.N. Westra, Vanadium (V) Equilibria : Thermodynamic Quantities for Some Protonation and Condensation Reactions, in: A.S. Tracey, D.C. Crans

(Eds.), Vanadium Compd. Chem. Biochem. Ther. Appl., American Chemical Society, Washington DC, 1998: pp. 51–59.

[24] J. Li, B. Hurley, R. Buchheit, Inhibition Performance Study of Vanadate on AA2024-T3 at High Temperature by SEM, FIB, Raman and XPS, J. Electrochem. Soc. 162 (2015) C219–C227. doi:10.1149/2.0371506jes.

[25] M. Iannuzzi, T. Young, G.S. Frankel, Aluminum Alloy Corrosion Inhibition by Vanadates, J. Electrochem. Soc. 153 (2006) B533. doi:10.1149/1.2358843.

[26] B.L. Hurley, S. Qiu, R.G. Buchheit, Raman Spectroscopy Characterization of Aqueous Vanadate Species Interaction with Aluminum Alloy 2024-T3 Surfaces, J. Electrochem. Soc. 158 (2011) C125–C131. doi:Doi 10.1149/1.3562557.

[27] Z. Feng, B. Hurley, J. Li, R. Buchheit, Corrosion Inhibition Study of Aqueous Vanadate on Mg Alloy AZ31, J. Electrochem. Soc. 165 (2018) C94–C102. doi:10.1149/2.1171802jes.

[28] N. Birbilis, R.G. Buchheit, Electrochemical Characteristics of Intermetallic Phases in Aluminum Alloys An Experimental Survey and Discussion, J. Electrochem. Soc. 152 (2005) B140–B151. doi:10.1149/1.1869984.

[29] N. Wang, J. Qiu, J. Wu, K. You, H. Luo, A Comparison of the Redox Properties of Bulk Vanadium Mixed Oxide Catalysts, Catal. Letters. 145 (2015) 1792–1797. doi:10.1007/s10562-015-1584-6.

[30] T. Kharlamova, E. Sushchenko, T. Izaak, O. Vodyankina, Phase composition, structural peculiarities and catalytic properties of supported MgO-V2O5/Al2O3 catalysts for oxidative dehydrogenation of propane: Insight into formation of surface Mg-V-O phase, Catal. Today. 278 (2016) 174–184. doi:10.1016/j.cattod.2016.05.006.

[31] G.T. Went, S.T. Oyama, A.T. Bell, Laser Raman Spectroscopy of Supported Vanadium Oxide Catalysts, J. Phys. Chem. 94 (1990) 4240–4246. doi:10.1021/j100373a067.

[32] L.J. Burcham, G. Deo, X. Gao, I.E. Wachs, In situ IR , Raman , and UV-Vis DRS spectroscopy of supported vanadium oxide catalysts during methanol oxidation, Top. Catal. 11–12 (2000) 85–100. doi:10.1023/A:1027275225668.

[33] P.S. Waleska, C. Hess, Oligomerization of Supported Vanadia: Structural Insight Using Surface-Science Models with Chemical Complexity, J. Phys. Chem. C. 120 (2016) 18510–18519. doi:10.1021/acs.jpcc.6b01672.

[34] D. Nitsche, C. Hess, Structure of Isolated Vanadia and Titania: A Deep UV Raman, UV-Vis, and IR Spectroscopic Study, J. Phys. Chem. C. 120 (2016) 1025–1037. doi:10.1021/acs.jpcc.5b10317.

[35] C. Zhang, Q. Yang, C. Koughia, F. Ye, M. Sanayei, S.J. Wen, S. Kasap, Characterization of vanadium oxide thin films with different stoichiometry using Raman spectroscopy, Thin Solid Films. 620 (2016) 64–69. doi:10.1016/j.tsf.2016.07.082.

[36] A.M. Amado, M. Aureliano, P.J.A. Riberio-Claro, J.J.C. Teixeira-Dias, Combined Raman and 51V NMR spectroscopic study of vanadium (V) oligomerization in aqueous alkaline solutions, J. Raman Spectrosc. 24 (1993) 699–703. doi:10.1002/jrs.1250241011.

[37] F. Ureña-Begara, A. Crunteanu, J.P. Raskin, Raman and XPS characterization of vanadium oxide thin films with temperature, Appl. Surf. Sci. 403 (2017) 717–727. doi:10.1016/j.apsusc.2017.01.160.

[38] G.I. Petrov, V. V. Yakovlev, J. Squier, Raman microscopy analysis of phase transformation mechanisms in vanadium dioxide, Appl. Phys. Lett. 81 (2002) 1023–1025. doi:10.1063/1.1496506.

[39] S.-H. Lee, H.M. Cheong, M. Je Seong, P. Liu, C.E. Tracy, A. Mascarenhas, J.R. Pitts, S.K. Deb, Microstructure study of amorphous vanadium oxide thin films using raman spectroscopy, J. Appl. Phys. 92 (2002) 1893. doi:10.1063/1.1495074.

[40] S. Hosseinpour, M. Johnson, Vibrational spectroscopy in studies of atmospheric corrosion, Materials. 10 (2017) 413. doi:10.3390/ma10040413.

[41] I.E. Wachs, J.-M. Jehng, G. Deo, B.M. Weckhuysen, V. V. Guliants, J.B. Benziger, In situ

Raman spectroscopy studies of bulk and surface metal oxide phases during oxidation reactions, Catal. Today. 32 (1996) 47–55. doi:10.1016/S0920-5861(96)00091-0.

[42] F. Zhang, T. Brinck, B.D. Brandner, P.M. Claesson, A. Dedinaite, J. Pan, In situ confocal Raman micro-spectroscopy and electrochemical studies of mussel adhesive protein and ceria composite film on carbon steel in salt solutions, Electrochim. Acta. 107 (2013) 276–291. doi:10.1016/j.electacta.2013.05.078.

[43] D.S. Kharitonov, I.I. Kurilo, I.M. Zharsky, Corrosion behavior of AMZ (AA3003) alloy in alkaline mediums with sodium orthovanadate addition, Sviridov Readings. 12 (2016) 117–128.

[44] I. Strydom, W. Za, A.G. Dormehl, Process for producing vanadyl/vanadous sulphate, 2004.

[45] D.J. Miller, M.C. Biesinger, N.S. McIntyre, Interactions of CO2 and CO at fractional atmosphere pressures with iron and iron oxide surfaces: One possible mechanism for surface contamination?, Surf. Interface Anal. 33 (2002) 299–305. doi:10.1002/sia.1188.

[46] M.A. Amin, N. El-Bagoury, M.H.H. Mahmoud, M.M. Hessien, S.S. Abd El-Rehim, J. Wysocka, J. Ryl, Catalytic impact of alloyed Al on the corrosion behavior of $Co_{50}Ni_{23}Ga_{26}Al_{1.0}$ magnetic shape memory alloy and catalysis applications for efficient electrochemical H_2 generation, RSC Adv. 7 (2017) 3635–3649. doi:10.1039/C6RA25384A.

[47] D.S. Kharitonov, I.B. Dobryden, B. Sefer, I.M. Zharskii, P.M. Claesson, I.I. Kurilo, Corrosion of AD31 (AA6063) Alloy in Chloride-Containing Solutions, Prot. Met. Phys. Chem. Surfaces. 54 (2018) 291–300. doi:10.1134/S2070205118020077.

[48] E. Heath, O.W. Howarth, Vanadium-51 and oxygen-17 nuclear magnetic resonance study of vanadate(V) equilibria and kinetics, J. Chem. Soc.{,} Dalt. Trans. (1981) 1105–1110. doi:10.1039/DT9810001105.

[49] L. Yin, Y. Jin, C. Leygraf, J. Pan, A FEM model for investigation of micro-galvanic corrosion of Al alloys and effects of deposition of corrosion products, Electrochim. Acta. 192 (2016) 310–318. doi:10.1016/j.electacta.2016.01.179.

[50] O. Guseva, J.A. Derose, P. Schmutz, Modelling the early stage time dependence of localised corrosion in aluminium alloys, Electrochim. Acta. 88 (2013) 821–831. doi:10.1016/j.electacta.2012.10.059.

[51] L. Yin, Y. Jin, C. Leygraf, N. Birbilis, J. Pan, Numerical Simulation of Micro-Galvanic Corrosion in Al Alloys: Effect of Geometric Factors, J. Electrochem. Soc. 164 (2017) C75–C84. doi:10.1149/2.1221702jes.

[52] U.G. Nielsen, A. Boisen, M. Brorson, C.J.H. Jacobsen, H.J. Jakobsen, J. Skibsted, Aluminum Orthovanadate (AlVO4): Synthesis and Characterization by 27 Al and 51 V MAS and MQMAS NMR Spectroscopy, Inorg. Chem. 41 (2002) 6432–6439. doi:10.1021/ic0204023.

[53] M.K. Atal, A. Saini, R. Gopal, M. Nagar, V. Dhayal, Synthesis and characterization of a new class of single-phase $AlVO_4$ precursors, Mater. Res. Innov. 8917 (2016) 1–5. doi:10.1080/14328917.2016.1198459.

[54] P. Buglyó, D.C. Crans, E.M. Nagy, R.L. Lindo, L. Yang, J.J. Smee, W. Jin, L.H. Chi, M.E. Godzala, G.R. Willsky, Aqueous chemistry of the vanadiumIII (VIII) and the VIII-dipicolinate systems and a comparison of the effect of three oxidation states of vanadium compounds on diabetic hyperglycemia in rats, Inorg. Chem. 44 (2005) 5416–5427. doi:10.1021/ic048331q.

[55] J. Orlikowski, J. Ryl, M. Jarzynka, S. Krakowiak, K. Darowicki, Instantaneous Impedance Monitoring of Aluminum Alloy 7075 Corrosion in Borate Buffer with Admixed Chloride Ions, CORROSION. 71 (2015) 828–838. doi:10.5006/1546.

[56] Z. Shaohong, F. Juan, S. Qiucheng, W. Liangpeng, L. Xinjun, In Situ Characterization on Thermal Transitions of VO2(B): Toward VO2(R) and V2O3, Rare Met. Mater. Eng. 45 (2016) 1374–1380. doi:10.1016/S1875-5372(16)30116-3.

[57] C. Tatsuyama, H. Fan, Raman scattering and phase transitions in V_{2}O_{3} and (V_{1-x}Cr_{x})_{2}O_{3}, Phys. Rev. B. 21 (1980) 2977–2983. doi:10.1103/PhysRevB.21.2977.
[58] Y. Bal, K.E. Bal, G. Cote, A. Lallam, Characterization of the solid third phases that precipitate from the organic solutions of Aliquat?? 336 after extraction of molybdenum(VI) and vanadium(V), Hydrometallurgy. 75 (2004) 123–134. doi:10.1016/j.hydromet.2004.07.004.
[59] G. Du, Z. Sun, Y. Xian, H. Jing, H. Chen, D. Yin, The nucleation kinetics of ammonium metavanadate precipitated by ammonium chloride, J. Cryst. Growth. 441 (2016) 117–123. doi:10.1016/j.jcrysgro.2016.02.016.
[60] S. Onodera, Y. Ikegami, Infrared and Raman Spectra of Ammonium, Potassium, Rubidium, and Cesium Metavanadates, Inorg. Chem. 125 (1980) 615–618.
[61] J. Zhang, J. Hu, L. Zhang, Raman Studies on Species in Single and Mixed Solutions of Molybdate and Vanadate, Chinese J. Chem. Phys. 29 (2016) 425–429. doi:10.1063/1674-0068/29/cjcp1604069.
[62] R.L. Frost, K.L. Erickson, M.L. Weier, O. Carmody, Raman and infrared spectroscopy of selected vanadates, Spectrochim. Acta - Part A Mol. Biomol. Spectrosc. 61 (2005) 829–834. doi:10.1016/j.saa.2004.06.006.
[63] P.S. Seetharaman, S. and Bhat, H. L. and Narayanan, Raman spectroscopic studies on sodium metavanadate, J. Raman Spectrosc. 14 (1983) 401--405. doi:jrs.1250140608.
[64] M.H. Kuok, S.H. Tang, Z.X. Shen, C.W. Ong, Raman Spectroscopic Studies of a-NaVO3, b=NaVO3 and NaVO3*2H20, 26 (1987) 6–12. doi:10.2174/1874067700802010006.
[65] A. Bouzidi, N. Benramdane, S. Bresson, C. Mathieu, R. Desfeux, M. El Marssi, X-ray and Raman study of spray pyrolysed vanadium oxide thin films, Vib. Spectrosc. 57 (2011) 182–186. doi:10.1016/j.vibspec.2011.07.003.
[66] A.N. Unnimaya, E.K. Suresh, R. Ratheesh, Crystal structure and microwave dielectric properties of new alkaline earth vanadate A4V2O9 (A=Ba, Sr, Ca, Mg and Zn) ceramics for LTCC applications, Mater. Res. Bull. 88 (2017) 174–181. doi:10.1016/j.materresbull.2016.12.026.
[67] X. Wu, J. Wang, S. Liu, X. Wu, S. Li, Study of vanadium(IV) species and corresponding electrochemical performance in concentrated sulfuric acid media, Electrochim. Acta. 56 (2011) 10197–10203. doi:10.1016/j.electacta.2011.09.006.
[68] L.E. Briand, J.M. Jehng, L. Cornaglia, A.M. Hirt, I.E. Wachs, Quantitative determination of the number of surface active sites and the turnover frequency for methanol oxidation over bulk metal vanadates, Catal. Today. 78 (2003) 257–268. doi:10.1016/S0920-5861(02)00350-4.
[69] H.D. Ruan, R.L. Frost, J.T. Kloprogge, Comparison of Raman spectra in characterizing gibbsite, bayerite, diaspore and boehmite, J. Raman Spectrosc. 32 (2001) 745–750. doi:10.1002/jrs.736.
[70] A.M. Amado, M. Aureliano, P.J.A. Riberio-Claro, J.J.C. Teixeira-Dias, Combined Raman and ’ ’ V NMR Spectroscopic, J. Raman Spectrosc. 24 (1993) 699–703.
[71] F. Rabello De Castro, Y. Lau Lam, M. Hawrylak Herbst, M. MacIel Pereira, T. Crispim Da Silva, N. Homs, P. Ramirez De La Piscina, VO2+ reaction with hydrotalcite and hydrotalcite-derived oxide: The effect of the vanadium loading on the structure of catalyst precursors and on the vanadium species, Eur. J. Inorg. Chem. (2013) 241–247. doi:10.1002/ejic.201200860.
[72] B.L. Hurley, K.D. Ralston, R.G. Buchheit, Corrosion Inhibition of Zinc by Aqueous Vanadate Species, J. Electrochem. Soc. 161 (2014) 471–475. doi:10.1149/2.0381410jes.
[73] M.A. Vuurmant, I.E. Wachs, In situ Raman spectroscopy of alumina-supported metal oxide catalysts, J. Phys. Chem. 96 (1992) 5008–5016. doi:10.1021/j100191a051.
[74] I.E. Wachs, Raman and IR studies of surface metal oxide species on oxide supports: Supported metal oxide catalysts, Catal. Today. 27 (1996) 437–455.

doi:http://dx.doi.org/10.1016/0920-5861(95)00203-0.
[75] E. Armstrong, M. Osiak, H. Geaney, C. Glynn, C. O'Dwyer, 2D and 3D vanadium oxide inverse opals and hollow sphere arrays, CrystEngComm. 16 (2014) 10804–10815. doi:10.1039/C4CE01797H.
[76] G. Yoganandan, J.N. Balaraju, Synergistic effect of V and Mn oxyanions for the corrosion protection of anodized aerospace aluminum alloy, Surf. Coatings Technol. 252 (2014) 35–47. doi:10.1016/j.surfcoat.2014.04.062.
[77] E. Hryha, E. Rutqvist, L. Nyborg, Stoichiometric vanadium oxides studied by XPS: Stoichiometric vanadium oxides studied by XPS, Surf. Interface Anal. 44 (2012) 1022–1025. doi:10.1002/sia.3844.
[78] J. Ryl, J. Wysocka, M. Jarzynka, A. Zielinski, J. Orlikowski, K. Darowicki, Effect of native air-formed oxidation on the corrosion behavior of AA 7075 aluminum alloys, Corros. Sci. 87 (2014) 150–155. doi:10.1016/j.corsci.2014.06.022.
[79] L. Kobotiatis, N. Pebere, P.G. Koutsoukos, Study of the electrochemical behaviour of the 7075 aluminum alloy in the presence of sodium oxalate, Corros. Sci. 41 (1999) 941–957. doi:10.1016/S0010-938X(98)00164-4.
[80] J. Wysocka, S. Krakowiak, J. Ryl, Evaluation of citric acid corrosion inhibition efficiency and passivation kinetics for aluminium alloys in alkaline media by means of dynamic impedance monitoring, Electrochim. Acta. 258 (2017) 1463–1475. doi:10.1016/j.electacta.2017.12.017.
[81] C.M. Abreu, M.J. Cristóbal, R. Figueroa, G. Pena, Passive layers developed on different tempers of AA7075 aluminium alloy after molybdenum implantation: XPS study of molybdenum implantation on AA7075 aluminium alloy, Surf. Interface Anal. 44 (2012) 1039–1044. doi:10.1002/sia.4860.
[82] M. Giza, P. Thissen, G. Grundmeier, Adsorption Kinetics of Organophosphonic Acids on Plasma-Modified Oxide-Covered Aluminum Surfaces, Langmuir. 24 (2008) 8688–8694. doi:10.1021/la8000619.
[83] Q. Liu, X. Tong, G. Zhou, H2O Dissociation-Induced Aluminum Oxide Growth on Oxidized Al(111) Surfaces, Langmuir. 31 (2015) 13117–13126. doi:10.1021/acs.langmuir.5b02769.
[84] S.B. Madden, J.R. Scully, Inhibition of AA2024-T351 Corrosion Using Permanganate, J. Electrochem. Soc. 161 (2014) C162–C175. doi:10.1149/2.075403jes.
[85] P. Pokorny, P. Tej, P. Szelag, Chromate conversion coatings and their current application, Metalurgija. 55 (2016) 253–256.
[86] M.W. Kendig, R.G. Buchheit, Corrosion inhibition of aluminum and aluminum alloys by soluble chromates, chromate coatings, and chromate-free coatings, Corrosion. 59 (2003) 379–400. doi:10.5006/1.3277570.
[87] O. Lopez-Garrity, G.S. Frankel, Corrosion Inhibition of Aluminum Alloy 2024-T3 by Sodium Molybdate, J. Electrochem. Soc. 161 (2013) C95–C106. doi:10.1149/2.044403jes.
[88] O. Lunder, J.C. Walmsley, P. MacK, K. Nisancioglu, Formation and characterisation of a chromate conversion coating on AA6060 aluminium, Corros. Sci. 47 (2005) 1604–1624. doi:10.1016/j.corsci.2004.08.012.
[89] E. McCafferty, Sequence of steps in the pitting of aluminum by chloride ions, Corros. Sci. 45 (2003) 1421–1438. doi:10.1016/S0010-938X(02)00231-7.
[90] C. Hess, G. Tzolova-Muller, R. Herbert, The influence of water on the dispersion of vanadia supported on silica SBA-15: A combined XPS and Raman study, J. Phys. Chem. C. 111 (2007) 9471–9479. doi:10.1021/jp0713920.
[91] X. Gao, S.R. Bare, B.M. Weckhuysen, I.E. Wachs, D. Plaines, V. Centrum, V. Opper, K.U. V Leu, In Situ Spectroscopic Investigation of Molecular Structures of Highly Dispersed Vanadium Oxide on Silica under Various Conditions, (1998) 10842–10852.
[92] S. Yamazaki, C. Li, K. Ohoyama, M. Nishi, M. Ichihara, H. Ueda, Y. Ueda, Synthesis,

structure and magnetic properties of V4O9-A missing link in binary vanadium oxides, J. Solid State Chem. 183 (2010) 1496–1503. doi:10.1016/j.jssc.2010.04.007.

[93] F. Zhang, J.-O. Nilsson, J. Pan, In Situ and Operando AFM and EIS Studies of Anodization of Al 6060: Influence of Intermetallic Particles, J. Electrochem. Soc. 163 (2016) C609–C618. doi:10.1149/2.0061610jes.

FIGURE CAPTIONS

Figure 1. (a–c) SEM micrographs showing the microstructure of the AA6063-T5 alloy with chemical information (EDX) provided for the Fe-Si-Mn intermetallic phase shown in (c).

Figure 2. (a) Volume fraction and (b) E-pH diagrams for an aqueous solution containing 3 mM $NaVO_3$ and 0.05 M NaCl. The volume fraction data were calculated without any external potential. The green dashed lines enclose the region of water stability.

Figure 3. SEM analyses before and after immersion in 0.05 M NaCl solution without vanadate inhibitor: (a, b) ETD images and (c, d) TLD images showing the surface of the specimen. The scale bar at the left also applies to the images at the right. Note the two fiducial marks, one on the top and the other on the bottom, in all three images in (a).

Figure 4. SEM analyses before and after immersion in 0.05 M NaCl solution with 3 mM $NaVO_3$ inhibitor. (a) ETD images and (b, c) TLD images showing the surface of the specimen. The scale bar at the left also applies to the images at the right. The arrows in panel (b) point towards an example of a surface precipitate site.

Figure 5. High-resolution XPS spectra registered in the binding energy range of (a) *V2p (b) Al2p* and (c) *O1s* at the surface of the analyzed sample. The spectra include results from the deconvolution model as thin solid lines, with the black solid line showing the overall fitting results. The sample was immersed in 0.05 M NaCl + 3 mM $NaVO_3$ solution for 6 hours.

Figure 6. Reference Raman spectra of solid vanadate compounds, with the oxidation state given in brackets: (a) V_2O_3 (V^{+3}), (b) VO_2 (V^{+4}), (c) V_2O_5 (V^{+5}), (d) NH_4VO_3 (V^{+5}), (e) $NaVO_3$ (V^{+5}), and vanadate-containing solutions: (f) $VO(SO_4)$ (V^{+4}), (g) 0.05 M NaCl + 3 mM $NaVO_3$ (V^{+5}).

Figure 7. (a) Optical micrographs of the AA6063-T5 surface exposed to 0.05 M NaCl + 3 mM $NaVO_3$ solution for 24 hours illustrating typical observations during the experiments. The dark color shows vanadate species adhering to the surface. Rinsing with deionized water exposes the IMP under the vanadate layer (b). The highlighted region shows the surface area selected for CRM examinations during *in-situ* (a) and *ex-situ* (b) measurements.

Figure 8. (a) *In-situ* optical micrograph of the AA6063-T5 surface after 6 hours of exposure to aqueous 0.05 M NaCl + 3 mM $NaVO_3$ solution, (b) Raman spectra of the detected surface components, local surface (c) and depth (d) components distribution images constructed from their characteristic Raman signals. In (c, d) yellow color represents compound with spectrum b1, red color compound with spectrum b2, green color compound with spectrum b3, and blue compound with spectrum b4. The dashed line in (a) shows where the Z-scan in panel d was conducted.

Figure 9. (a) *In-situ* optical micrograph of the AA6063-T5 surface after 24 hours of exposure to aqueous 0.05 M NaCl + 3 mM $NaVO_3$ solution, (b) Raman spectra of the detected surface components, local surface (c) and depth (d) components distribution images constructed from their characteristic Raman signals. In (c, d) red color represents compound with spectrum b1 and green color compound with spectrum b2. The dashed line in (a) shows where the Z-scan in panel d was conducted.

Figure 10. Optical micrographs (a, d), *ex-situ* Raman spectra of the detected surface components (b, e), and local components distribution images constructed from their characteristic Raman signals (c, f), obtained immediately after removal from the solution (a–c) and after 24 hours of aging in air (d–f). In (c) green color represents compound with spectrum b1 and red color compound with spectrum b2. In (f) red color represents compound with spectrum in (e). The samples were immersed in 0.05 M NaCl + 3 mM $NaVO_3$ solution for 24 hours and gently rinsed by deionized water before being analyzed.

Figure 11. Schematic illustration of the vanadate film formation process on the surface of the AA6063-T5 alloy.

Figures

FIGURE 1

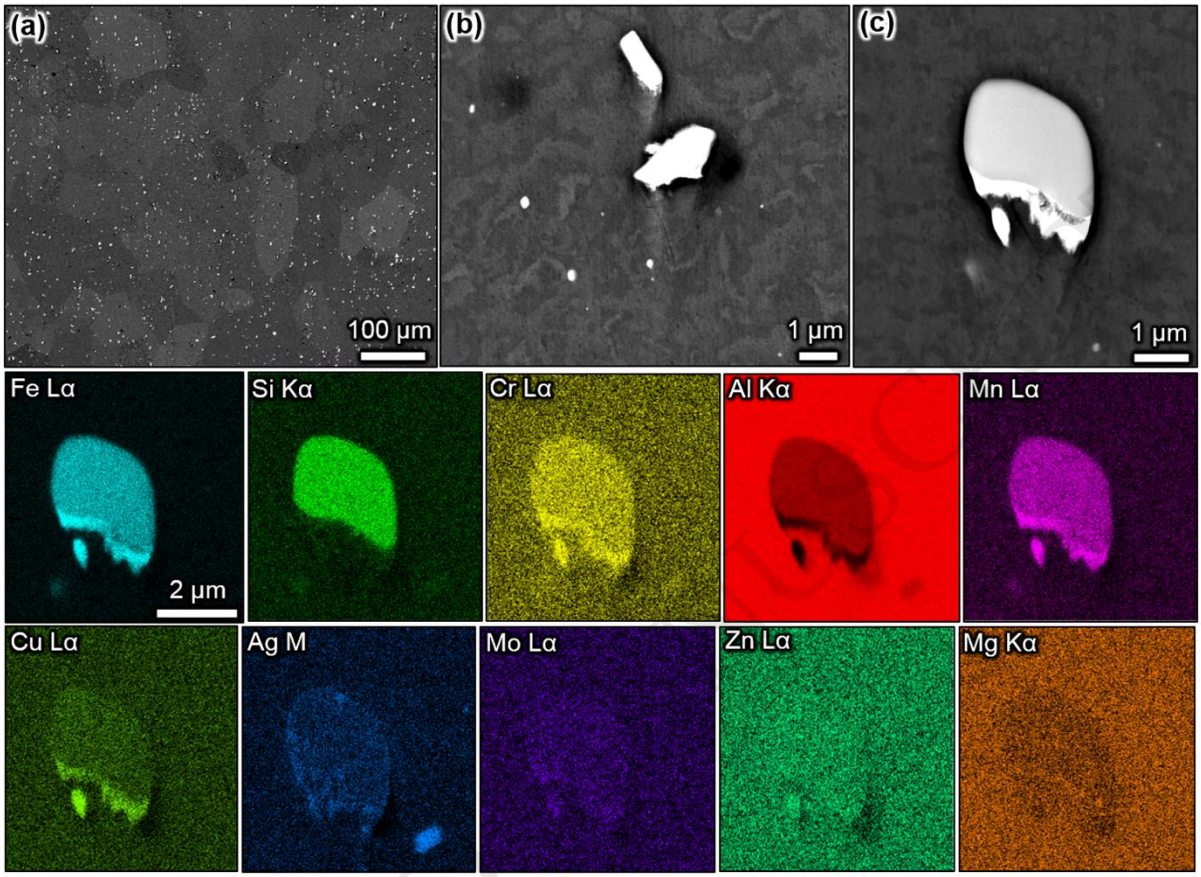

FIGURE 2

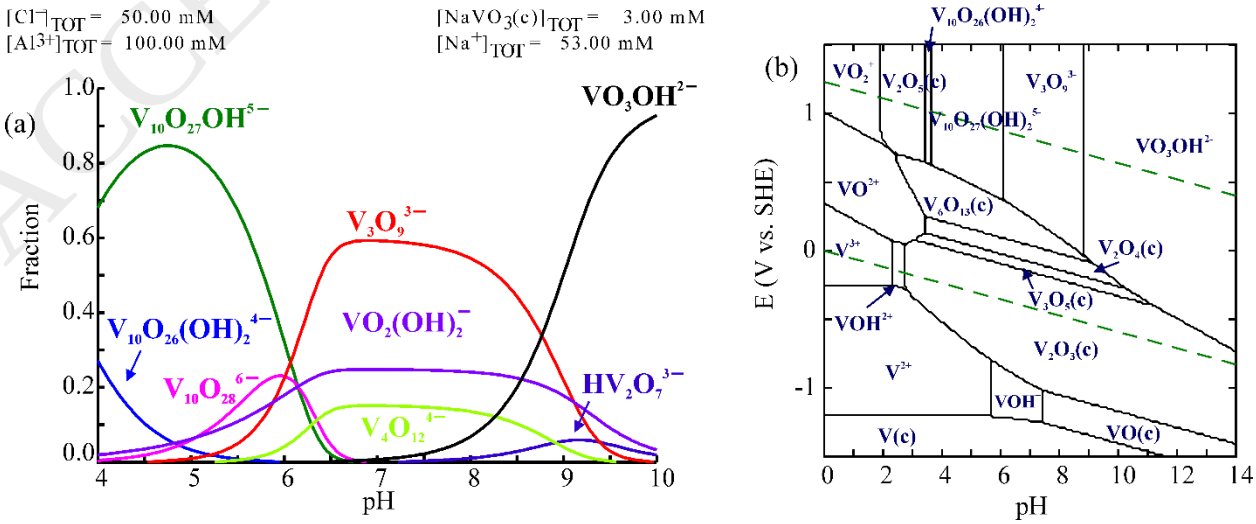

FIGURE 3

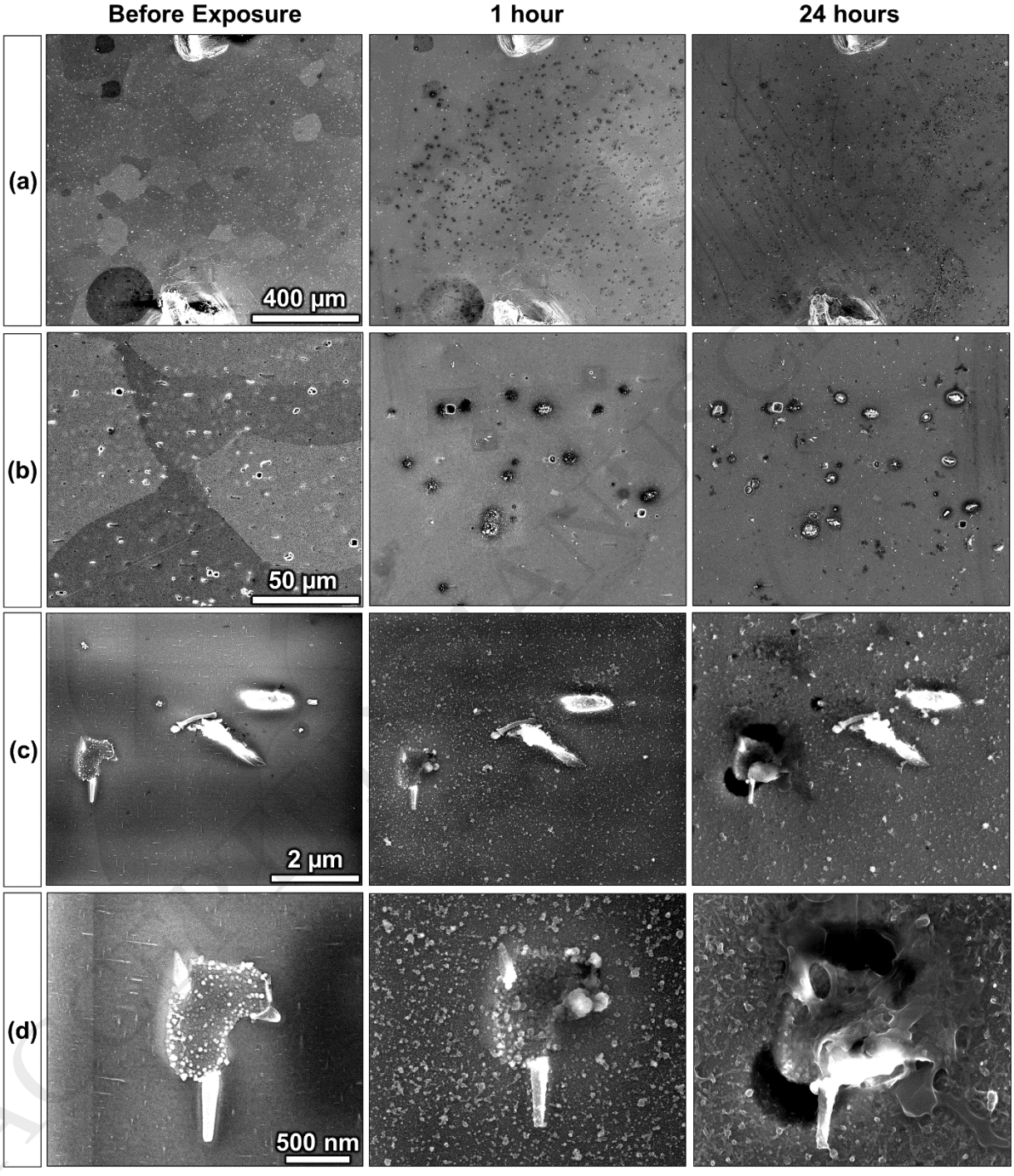

FIGURE 4

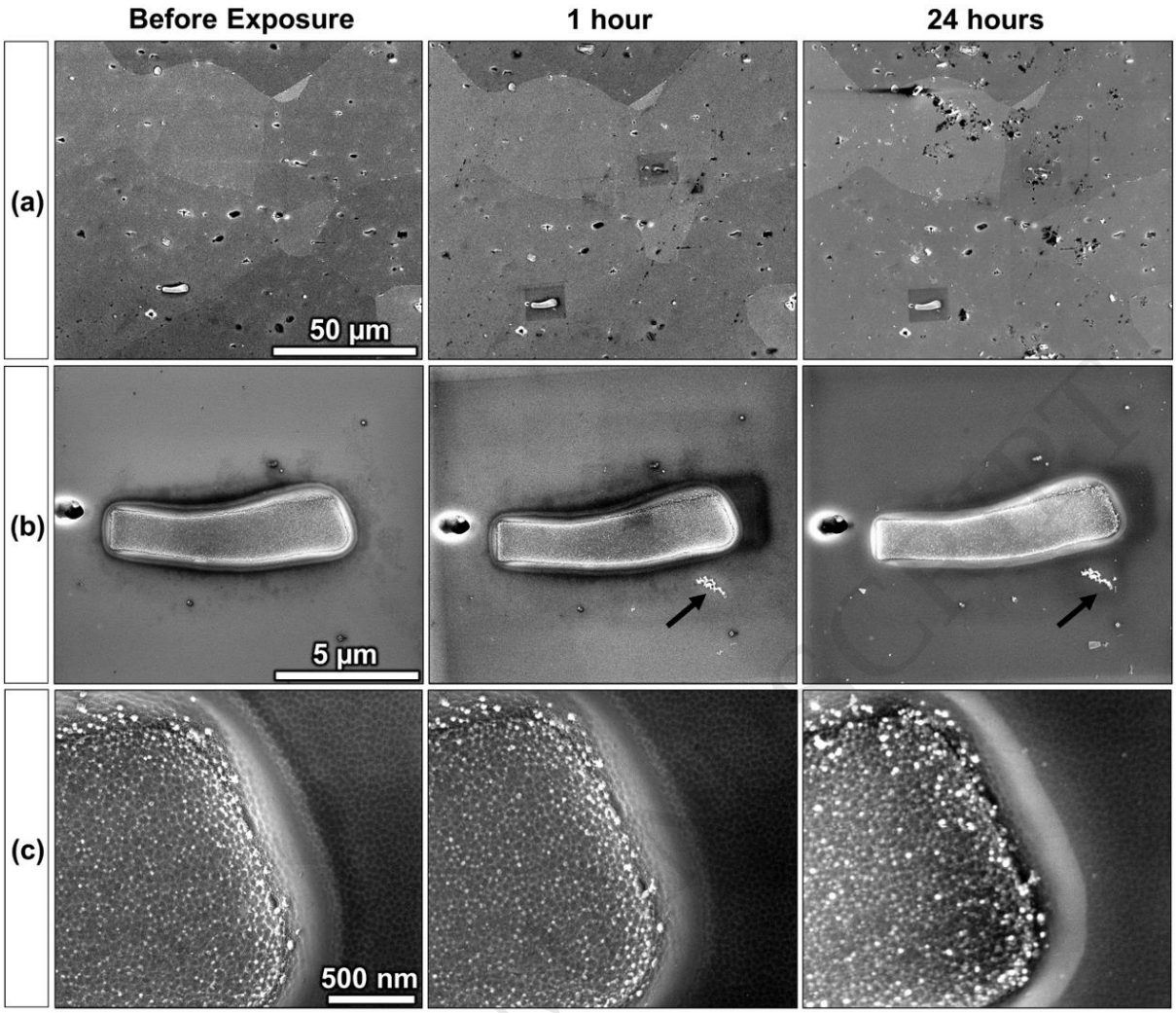

FIGURE 5

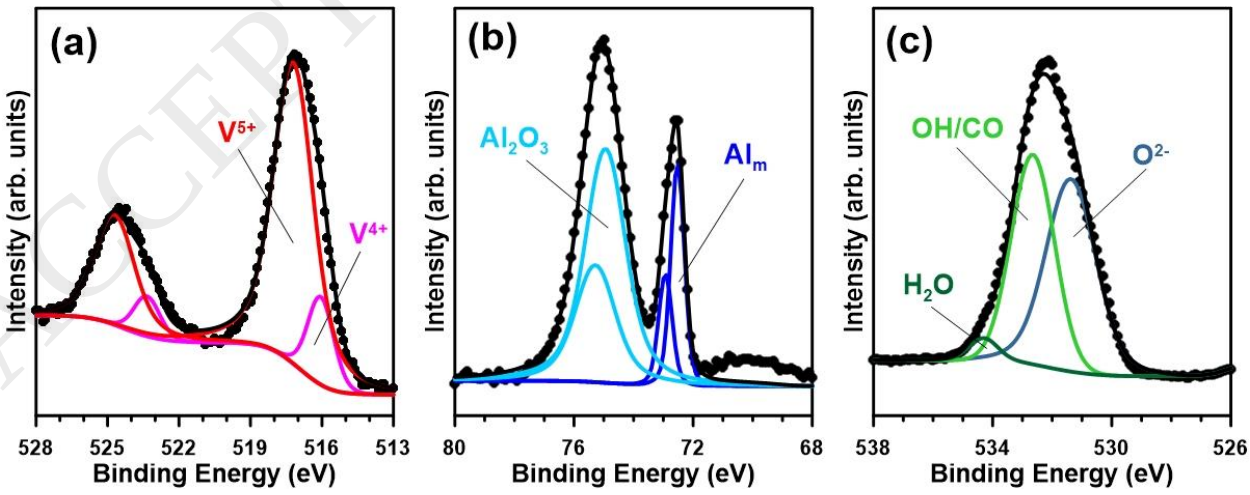

FIGURE 6

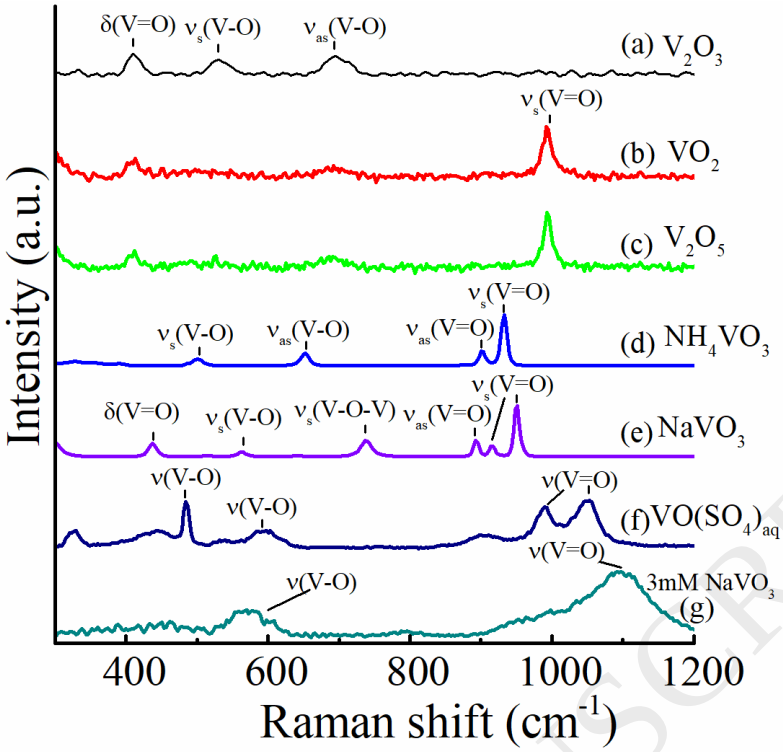

FIGURE 7

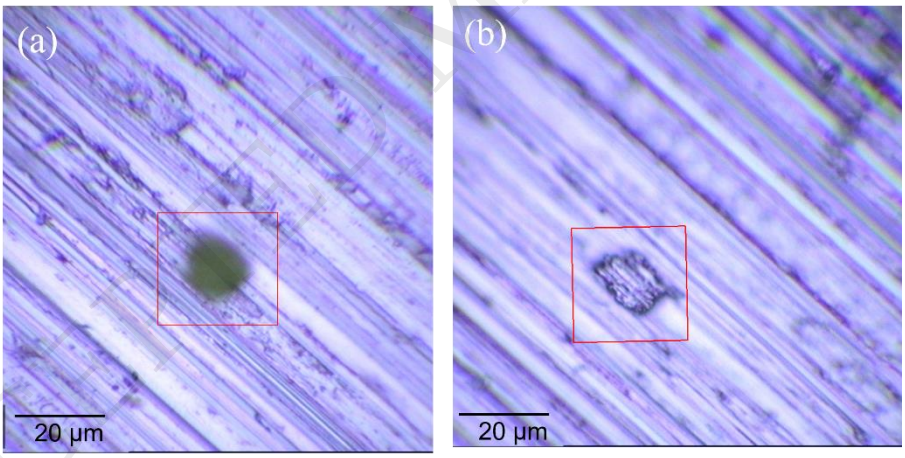

FIGURE 8

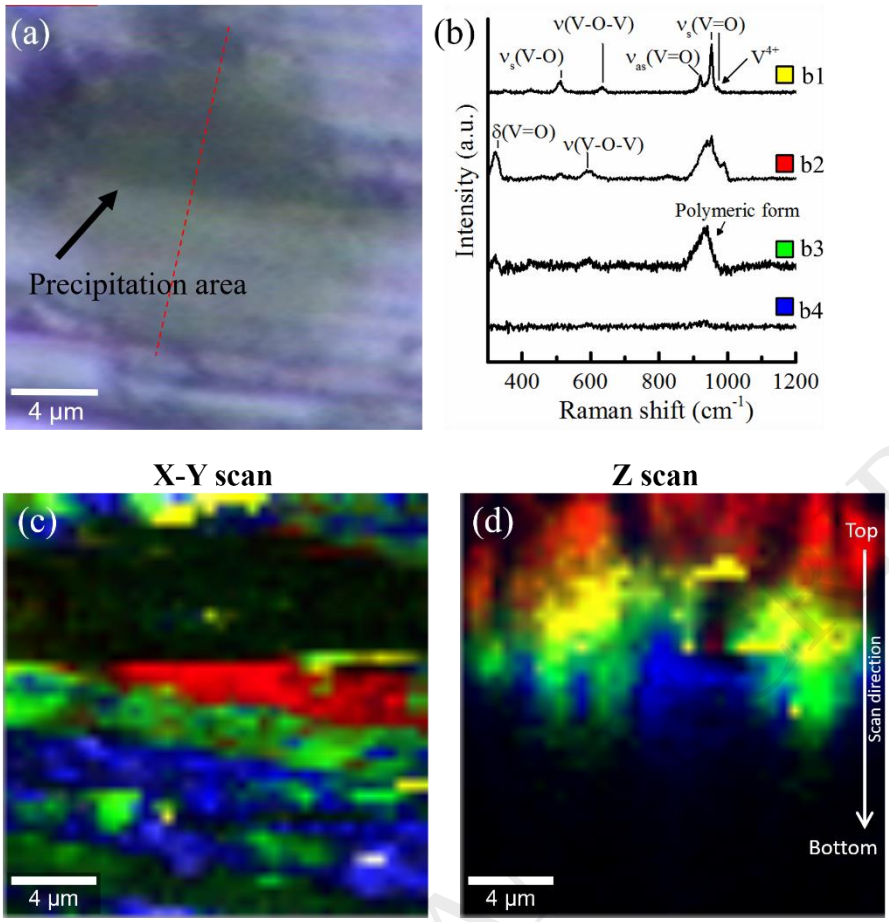

FIGURE 9

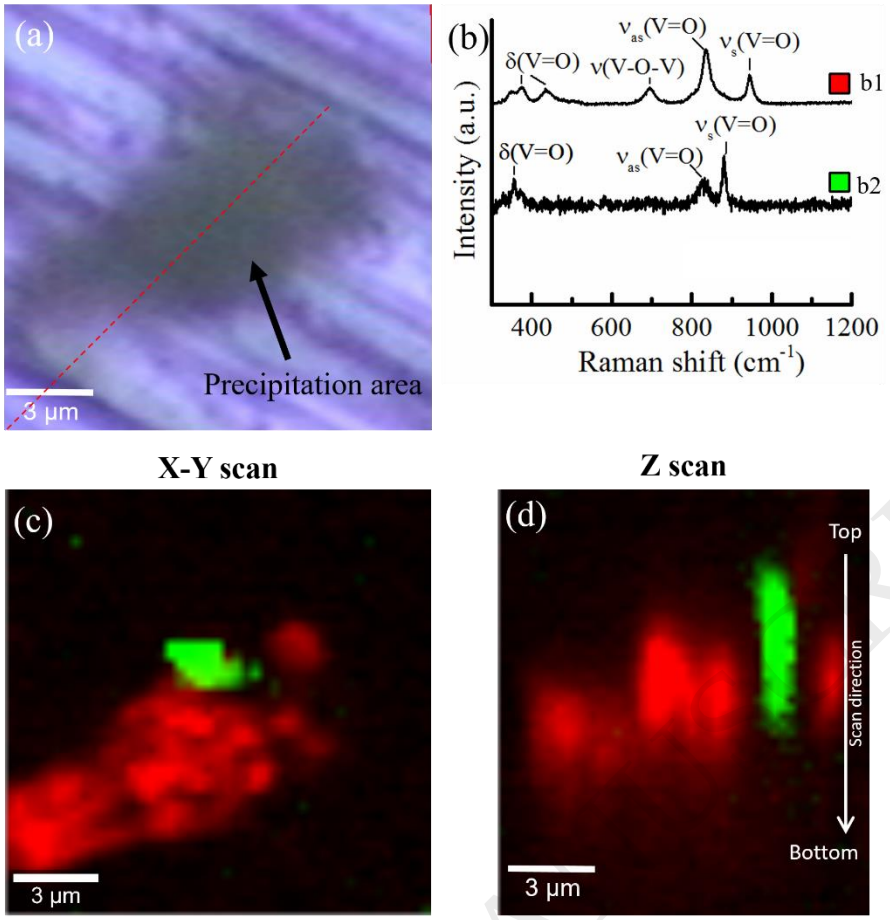

FIGURE 10

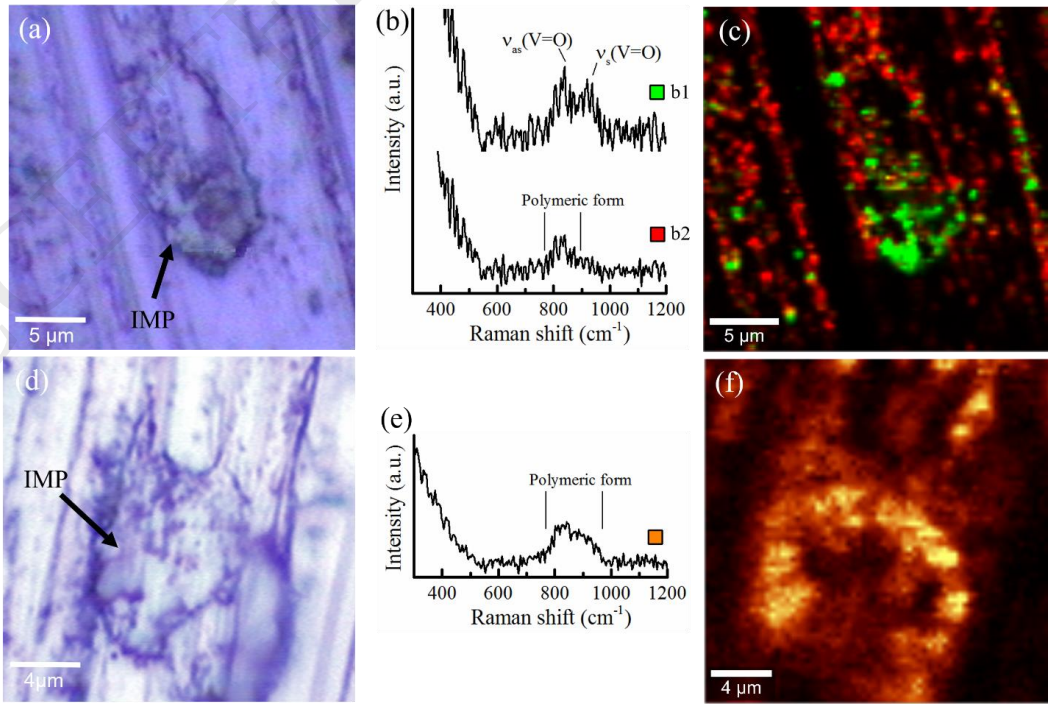

FIGURE 11

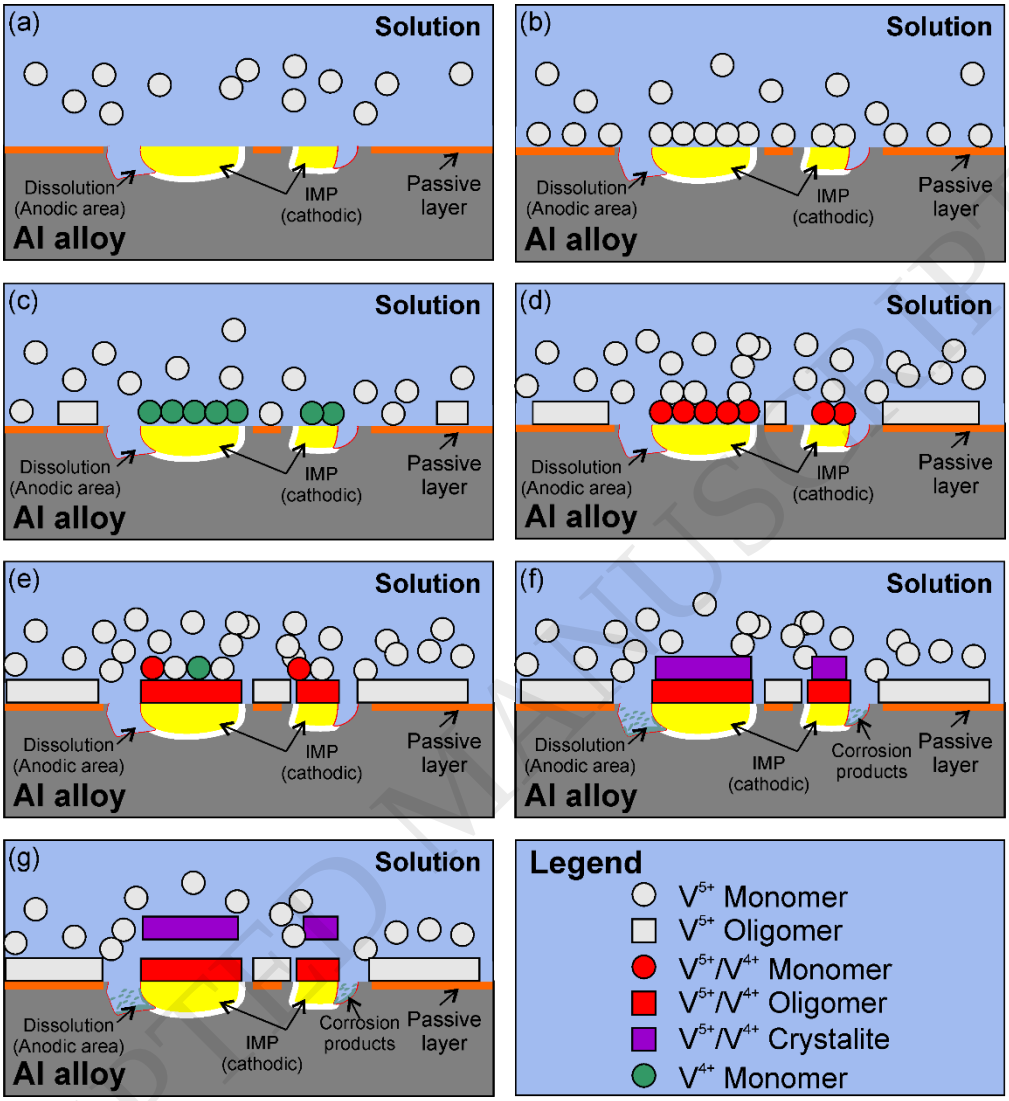

TABLES

Table 1. Surface chemical composition estimated from high-resolution XPS analysis in BE range of the Al2p, V2p and O1s photoelectron peaks. The sample was immersed in 0.05 M NaCl + 3 mM $NaVO_3$ solution for 6 hours prior to analysis in vacuum.

Analyzed peak	Chemical state	BE (eV)	Contribution (atom %)
Al2p$^{3/2}$	Al^0	72.5	7.1
	Al_2O_3	75.0	25.2
V2p$^{3/2}$	V (V)	517.2	5.2
	V (IV)	516.0	0.8
O1s	O^{2-}	531.7	31.4
	OH^-	532.7	28.1
	H_2O	534.3	2.2

Table 2. Raman band positions (cm^{-1}) of solid (s) and aqueous (aq) vanadium species.

Formula	*Aggregate*	*V–O–V*				*V=O*	*Ref*
		ν Symmetric	*ν Asymmetric*	*δ*	*Not specified*		
Vanadium (III)							
V_2O_3	s				995, 694, 530, 494, 410		This paper
V_2O_3	s				589, 501, 412, 328, 295, 239, 213		[56]
V_2O_3	s				595, 501, 327, 290, 234, 210		[57]
Vanadium (IV)							
VO_2	s				993, 686, 410		This paper
VO_2	s				993, 697, 524, 480,402		[26]
VO_2	s				612, 497, 392, 308, 221, 191, 142		[38]
VO^{2+}	s				650, 460, 310	1001, 972	[67]
VO^{2+}	aq				990, 904, 594, 537, 485, 445, 326		This paper
V_4O_9	s	1000	693	501, 258, 231,	139, 119		[65]
Vanadium (V)							
V_2O_5	s				994, 694, 526, 409		This paper
V_2O_5	s				703, 527, 485, 405, 305, 283	997	[31]
V_2O_5	s				920, 800, 600, 550	1028	[41]
α-$NaVO_3$	s	507, 547	634	376, 358, 344, 253	955, 940		[64]
β-$NaVO_3$	s	557, 431	737	257, 203	948, 911, 887, 288		[63]
$NaVO_3$	s				950, 915, 893, 738, 563, 437, 294		This paper
NH_4VO_3	s				932, 902, 473		This paper
NH_4VO_3	s	647	496	260, 210		928, 898, 385	[59]
$AlVO_4$	s	986, 923	880, 893	414		1006	[29]
$AlVO_4$	s				991, 954, 926,	1020	[68]

					907, 853, 569, 406, 329,		
$FeVO_4$	s				969, 934, 899, 850, 738, 773, 663, 500,		[68]
MgV_2O_6	s				836, 730, 452, 265, 174	952	[30]
CaV_2O_6	s	537, 474, 359	886, 871, 750, 704		933	953	[62]
$Mg_3V_2O_8$	s	881, 861, 845, 826	517	349	273, 116		[66]
$Mg_4V_2O_9$	s	859, 823		337	272, 197, 142		[66]
$Mg_3(VO_4)_2$	s				859, 834, 357, 284, 149		[68]
$Cu_3(VO_4)_2$	s				867, 805, 368, 316	1020	[68]
$NaVO_3$ (3 mM)	aq				500–640 (wide), 900–1200 (wide)		This paper
$(VO_3)_n^{n-}$	aq	945	905		630, 540, 490, 330		[60]
$(VO_3)_n^{n-}$	aq	830	464		947, 840, 627, 475	988	[61]
$V_4O_{12}^{4-}$	aq		947 (strongest band)				[18]
$V_{10}O_{28}^{6-}$	aq				967, 835, 454	994	[61]
$V_{10}O_{28}^{6-}$	aq				967, 593, 315	995	[18]
$HV_{10}O_{28}^{5-}$					835, 454	994	[61]